JGR Space Physics

RESEARCH ARTICLE
10.1029/2024JA033178

Key Points:

- TIEGCM-ICON is used to quantify the impact of the upward-propagating tidal spectrum on thermospheric intra-seasonal oscillations (ISOs)
- Thermospheric mean zonal winds exhibit prominent (±20 m/s) tidally driven ISOs largest at low latitudes near 110–150 km altitude
- Correlation and Hovmöller analyses demonstrate a strong connection with the tropospheric Madden-Julian Oscillation

Correspondence to:
F. Gasperini,
federico.gasperini@arcfield.com

Citation:
Gasperini, F., Maute, A., Wang, H., McClung, O., Aggarwal, D., & Kumari, K. (2025). Tidally driven intra-seasonal oscillations in the thermosphere from TIEGCM-ICON and connections to the Madden-Julian Oscillation. *Journal of Geophysical Research: Space Physics*, *130*, e2024JA033178. https://doi.org/10.1029/2024JA033178

Received 14 AUG 2024
Accepted 9 JAN 2025

Author Contributions:
Conceptualization: Federico Gasperini
Data curation: Federico Gasperini
Formal analysis: Federico Gasperini
Funding acquisition: Federico Gasperini
Investigation: Federico Gasperini
Methodology: Federico Gasperini, Houjun Wang
Project administration: Federico Gasperini
Resources: Federico Gasperini, Owen McClung, Komal Kumari
Software: Federico Gasperini
Supervision: Federico Gasperini
Validation: Federico Gasperini
Visualization: Federico Gasperini, Houjun Wang, Deepali Aggarwal
Writing – original draft: Federico Gasperini
Writing – review & editing: Astrid Maute, Deepali Aggarwal, Komal Kumari

Tidally Driven Intra-Seasonal Oscillations in the Thermosphere From TIEGCM-ICON and Connections to the Madden-Julian Oscillation

Federico Gasperini[1], Astrid Maute[2], Houjun Wang[1], Owen McClung[1,3], Deepali Aggarwal[4], and Komal Kumari[5]

[1]Orion Space Solutions, Louisville, CO, USA, [2]CIRES, University of Colorado, Boulder, CO, USA, [3]Ann and H.J. Smead Aerospace Engineering Sciences, University of Colorado, Boulder, CO, USA, [4]Department of Physics and Astronomy, Clemson University, Clemson, SC, USA, [5]High Altitude Observatory, National Center for Atmospheric Research, Boulder, CO, USA

Abstract Recent evidence has revealed that strong coupling between the lower atmosphere and the thermosphere (>100 km) occurs on intra-seasonal (IS) timescales (~30–90 days). The Madden-Julian Oscillation (MJO), a key source of IS variability in tropical convection and circulation, influences the generation and propagation of atmospheric tides and is believed to be a significant driver of thermospheric IS oscillations (ISOs). However, limited satellite observations in the "thermospheric gap" (100–300 km) and challenges faced by numerical models in characterizing this region have hindered a comprehensive understanding of this connection. This study uses an Ionospheric Connection Explorer (ICON)-adapted version of the Thermosphere Ionosphere Electrodynamics General Circulation Model, incorporating lower boundary tides from Michelson Interferometer for Global High-resolution Thermospheric Imaging (MIGHTI) observations, to quantify the impact of the upward-propagating tidal spectrum on thermospheric ISOs and elucidate connections to the MJO. Thermospheric zonal and diurnal mean zonal winds exhibit prominent (~20 m/s) tidally driven ISOs throughout 2020–2021, largest at low latitudes (±30°) near 110–150 km altitude. Correlation analyses confirm a robust connection ($r > 0.6$) between thermospheric ISOs, tides, and the MJO. Additionally, Hovmöller diagrams show eastward tidal propagation consistent with the MJO and concurrent Sounding of the Atmosphere using Broadband Emission Radiometry (SABER) observations. This study demonstrates that vertically propagating tides play a crucial role in linking IS variability from the lower atmosphere to the thermosphere, with the MJO identified as a primary driver of this whole-atmosphere teleconnection. Understanding these connections is vital for advancing our knowledge in space physics, particularly regarding the dynamics of the upper atmosphere and ionosphere.

Plain Language Summary In recent years, scientists have discovered how weather systems in Earth's lower atmosphere, particularly in the tropics, influence the upper atmosphere. The thermosphere (90–600 km above Earth) and ionosphere (a region of charged particles within the thermosphere) are especially affected by solar tides—atmospheric waves from sunlight, enhanced by tropical weather systems like deep convection. One major driver of these tides is the Madden-Julian Oscillation (MJO), a tropical weather pattern bringing bursts of rain and thunderstorms. We used a numerical model called TIE-GCM to examine how the MJO drives variations in the thermosphere through these tides. Our analysis focused on altitudes between 110 and 150 km near the equator, finding large, periodic changes in east-west winds, exceeding 20 m/s. These wind variations align with solar tide changes, matching the MJO's timing and movement. Observations from other satellite missions support our findings. This work demonstrates how lower atmospheric processes (below about 20 km) influence the thermosphere, with the MJO as a key driver connecting surface weather to upper-atmosphere behavior. Understanding these connections is vital for improving space weather predictions, which affect satellites and communication systems.

1. Introduction

The structure and dynamics of the thermosphere, spanning altitudes of approximately 100–500 km, are influenced by external processes associated with the Sun and magnetosphere (e.g., Johnson & Heelis, 2005; Thayer & Semeter, 2004), as well as internal processes related to atmospheric waves propagating from the lower atmosphere (Andrews et al., 1987). These waves are characterized by different spatiotemporal scales and include

global-scale solar tides, planetary waves, and Kelvin waves, as well as smaller-scale gravity waves (e.g., Fritts & Alexander, 2003; Forbes et al., 2009; Gasperini et al., 2015; Liu, 2016; Pancheva et al., 2012; Yiğit & Medvedev, 2015). Of particular interest in understanding the thermosphere's dynamics, known to vary significantly from intra-seasonal (IS) to inter-annual time scales (e.g., Sassi et al., 2019), is the role of upward-propagating solar tides (e.g., Gasperini & Oberheide, 2024 and references therein). Emerging modeling and space-based evidence suggest that much of the IS variability of the thermosphere is connected with an IS-modulated vertically propagating tidal spectrum (e.g., Gasperini et al., 2017a, 2020; Kumari et al., 2020, 2021; Li & Lu, 2020, 2021; Vergados et al., 2018; Yang et al., 2018).

Solar tides are persistent and ubiquitous global-scale oscillations observed in various atmospheric fields, such as wind, temperature, pressure, density, and geopotential height, with periods that are integer fractions of a solar day (Chapman & Lindzen, 1970; Forbes, 1995; Hagan et al., 1995; Matsushita, 1967a, 1967b). The notation DWs or DEs is used to describe westward or eastward-propagating diurnal tides, respectively, with zonal wavenumber "s." For semidiurnal tides, "S" replaces "D," while zonally symmetric oscillations are denoted as D0 and S0. Solar tides can be excited through several mechanisms, including the absorption of solar radiation, large-scale latent heat release from deep convective clouds in the troposphere, the gravitational pull of the Sun, and secondary waves resulting from nonlinear wave-wave interactions (Chang et al., 2011; Forbes et al., 2021a, 2021b; Gasperini & Oberheide, 2024; Gasperini et al., 2015, 2021, 2022; Liu, 2016; Palo et al., 1999).

The MJO (Madden & Julian, 1971, 1994) represents the principal mode of IS variability in tropical convection and circulation and has been a focus of extensive research since its discovery due to its critical role in medium-range weather forecasting. Characterized as an eastward-moving disturbance within low latitudes ($\pm 30°$) , the MJO typically recurs every 30–90 days, influencing tropical winds, clouds, rainfall, and numerous other atmospheric variables (Zhang, 2005). The Real-time Multivariate MJO series 1 (RMM1) and 2 (RMM2) indices (Wheeler & Hendon, 2004) are commonly used to identify the MJO. This oscillation generates a spectrum of global-scale waves, predominantly through convective forcing (Wheeler & Kiladis, 1999), and exhibits significant dependence on season MJO magnitude, and phase. Despite the rapid attenuation of the MJO above the tropopause due to its low frequency and slow zonal propagation speed (e.g., Tian et al., 2012; Zhang, 2005), its impacts have been observed in lower thermospheric gravity waves (e.g., Eckermann et al., 1997; Karoly et al., 1996; Li & Lu, 2020, 2021; Moss et al., 2016) and solar tides (e.g., Gasperini et al., 2017a, 2020; Kumari et al., 2020, 2021; Vergados et al., 2018, 2020; Yang et al., 2018). Early investigations into MJO signals within the lower thermosphere were limited and predominantly based on radar wind observations. Eckermann et al. (1997) and Lieberman (1998) suggested that while the MJO is confined to the lower atmosphere, it could modulate upward propagating tides and gravity waves, potentially inducing similar periodic signatures across various vertical levels. Subsequently, Lieberman et al. (2007) proposed that this whole atmosphere IS coupling involving tidal variability can occur through several mechanisms: variability in tropospheric heating that generates the tides; interactions with the zonal mean flow, which modulate tidal behavior as waves propagate through a variable background in the middle and upper atmosphere; or nonlinear wave-wave interactions.

As noted above, the influence of the MJO on tides and the related effects on the thermosphere were first suggested over two decades ago. However, only recent advancements in satellite observational capabilities and physics-based models have enabled improved quantification and characterization of these effects. Satellite-based thermospheric observations (e.g., Gasperini et al., 2017a, 2020; Kumari et al., 2020; Li et al., 2024) and modeling efforts (e.g., Gasperini et al., 2020; Kumari et al., 2021; Vergados et al., 2018; Yang et al., 2018) have demonstrated a robust connection between solar tides in the thermosphere and the tropospheric MJO. Using cross-track wind measurements from the Challenging Minisatellite Payload (CHAMP) and the Gravity field and steady-state Ocean Circulation Explorer (GOCE) satellites, along with high-resolution Thermosphere-Ionosphere-Mesosphere-Electrodynamics General Circulation Model (TIME-GCM) simulations forced with Modern-Era Retrospective Analysis for Research and Applications (MERRA) reanalysis data, and Outgoing Longwave Radiation (OLR) data, Gasperini et al. (2017a) identified significant 90-day oscillations in thermospheric zonal mean and DE3 zonal winds during 2009–2010, linking these oscillations to variability in tropospheric convective activity. Following this study, Vergados et al. (2018) used 14 years of Sounding of the Atmosphere using Broadband Emission Radiometry (SABER) temperature measurements to show distinct IS oscillations (ISO) in the low-latitude lower thermosphere and connections to tides. Kumari et al. (2020) showed that the MJO influences the DE3 and DW1 temperature tides in the lower thermosphere by $\sim$25% and $\sim$10% (peak-to-peak), respectively. Their findings indicated a strong seasonal dependency of the MJO influence, with

Kumari et al. (2020) observing robust effects across all seasons, dependent on the MJO phase and location. Moreover, they observed that the seasonal variations in the IS variability of nonmigrating tides at various MJO locations were found to be more pronounced than those in migrating diurnal tides. Further investigation by Kumari et al. (2021), using Specified-Dynamics Whole Atmosphere Community Climate Model with thermosphere and ionosphere extension (SD/WACCM-X), found that IS variability in tidal heating plays a more crucial role than tidal amplitude modulation by background winds in imprinting the MJO signal on low-latitude lower thermospheric tides. There is observational evidence of MJO modulation not only of thermospheric tides but also of the zonal and diurnal mean (ZDM) winds, with variations of approximately 20 m/s peak-to-peak (amplitude difference between consecutive maxima and minima in the wind speed variations caused by the MJO), as shown by satellite diagnostics from CHAMP and GOCE (Gasperini et al., 2017a, 2020). The MJO's influence extends well into the thermosphere, as evidenced by in-situ wind observations near 260 km from the GOCE satellite.

These recent studies highlight significant coupling between the troposphere and thermosphere on IS timescales, prompting critical questions with broad implications for the entire atmospheric system. Understanding the connection between the MJO and the upward-propagating tidal spectrum, and the impact of the MJO-modulated wave spectrum on the thermosphere, is a crucial next step for improving whole atmosphere prediction capabilities. Further investigation of the IS variability of the thermosphere and connections to the MJO is thus warranted. In light of these considerations, two major goals addressed by this study are (a) to better understand the role that tidal variability from the lower and middle atmosphere plays in producing thermospheric zonal wind ISOs, and (b) to examine connections between thermospheric winds, tidal variability, and the tropospheric MJO. These advancements are crucial to achieving an improved understanding of the coupling between terrestrial weather and variability in the "entangled" thermosphere-ionosphere (T-I) system.

This paper is structured as follows: Section 2 introduces the data and model used; Section 3 contains a brief description of the methods and techniques employed; Section 4 presents the results; and Section 5 summarizes the main conclusions of the study.

2. Data and Model

2.1. OLR

The daily Outgoing Longwave Radiation (OLR) Climate Data Record (CDR) quantifies the amount of infrared radiation emitted from the Earth's surface and lower atmosphere into space, providing insights into cloud cover and water vapor distribution (Gruber & Winston, 1978). Since 1979, this record has primarily used data from high-resolution infrared radiation sounders, supplemented by newer technologies such as the Infrared Atmospheric Sounding Interferometer since 2007 and the Cross-track Infrared Sounder (CrIS) since 2012. To enhance accuracy, OLR data is also derived from operational geostationary imagers, integrating multiple sources through statistical methods like OLR regression, prediction coefficients for instrument temperature, and corrections for inter-satellite biases. The data set to be used for this study ("olr.day.mean.nc" product) consists of daily OLR values binned in a 2.5° latitude x 2.5° longitude global grid with gaps that are temporally and spatially interpolated (Liebmann & Smith, 1996). OLR estimation algorithms have an accuracy of about 4–8 Wm^{-2} (Kayano et al., 1995).

2.2. RMM MJO Index

The Real-time Multivariate MJO (RMM) index is used to monitor the MJO. MJO events are commonly identified using RMM series 1 (RMM1) and series 2 (RMM2), as detailed in Wheeler and Hendon (2004). The RMM index identifies the strength and position of the MJO's active phase, characterized by extensive and persistent cloudiness typically observed in the Indian Ocean region. Comprising the first two principal components derived from OLR, 850-hPa zonal wind, and 200-hPa zonal wind averaged between 15° S and 15° N, the RMM index provides a quantitative measure of the MJO's intensity and location within the tropics. MJO events are grouped into eight active phases (Phases 1–8) according to the amplitude and phase information obtained by combining the RMM1 and RMM2 values, with enhanced convection moving eastward from the central Pacific to the Indian Ocean. An "active" MJO event is said to occur when an RMM index is greater than 1 for at least 5 consecutive days. This study presents correlative findings using RMM1 as a proxy for MJO variability, given its highest correlation with thermospheric parameters. Notably, similar conclusions can be derived when using MJO amplitude or RMM2.

Investigating the underlying causes for the stronger correlations observed with RMM1, as opposed to RMM2 and MJO amplitude, is beyond the scope of this work.

2.3. ICON/MIGHTI

ICON is a Heliophysics System Observatory mission with the primary objective to observe how the ionosphere is influenced by the dynamics of the neutral atmosphere (Immel & Eastes, 2019; Immel et al., 2018, 2021). ICON was launched on 10 October 2019 on a nearly circular ∼27° inclination orbit near 590 km altitude, providing concurrent measurements of the thermospheric and ionospheric environments through 10 November 2022. Operating as a single observatory, ICON collected data covering two local solar times (LST) per day at a particular latitude, each progressing approximately 29.8 min earlier daily. ICON's Michelson Interferometer for Global High-resolution Thermospheric Imaging (MIGHTI) instrument provides day and night vector winds with a precision of ∼8.7 m/s (Harding et al., 2021, 2024) and temperatures with uncertainty of around 7 K (Stevens et al., 2022) in the ∼94–105 km altitude region (L2 v05).

2.4. TIMED/SABER

The Thermosphere Ionosphere Mesosphere Energetics Dynamics (TIMED) satellite was launched in December 2001 into a circular orbit near 625 km altitude with a ∼74° inclination (Russell et al., 1999). Sounding of the Atmosphere using Broadband Emission Radiometry (SABER) is a limb-scanning infrared radiometer onboard TIMED, operating with 10 broadband channels spanning 1.27–17 μm. SABER retrieves kinetic temperatures from CO_2 emissions at 15 μm and 4.3 μ m wavelengths, covering altitudes from roughly 20–120 km (Mertens et al., 2003). The retrieval errors are ±1–2 K below ∼70 km, with an additional error of ∼1.4 K at higher altitudes due to nonlocal thermodynamic equilibrium (non-LTE) effects (Remsberg et al., 2008). Here, we will use SABER temperature data (v2.0 Level 2). This data set provides global coverage in one day and captures two different local times (LTs) for any given latitude.

2.5. TIEGCM-ICON

The Thermosphere-Ionosphere-Electrodynamics General Circulation Model (TIEGCM) developed by the National Center for Atmospheric Research's High-Altitude Observatory, is a first-principle, time-dependent, three-dimensional self-consistent numerical model of the thermosphere (Dickinson, 1984; Qian et al., 2014; Richmond et al., 1992; Roble et al., 1988), which includes the dynamics, energetics and chemistry with a steady-state ionospheric electrodynamo in a realistic geomagnetic main field defined by the International Geomagnetic Reference Field (IGRF-13) (Alken et al., 2021). The initial developments of the TIEGCM can be traced back to seminal works by Dickinson (1984), Roble et al. (1988), and Richmond et al. (1992). Advancements are documented in studies such as Qian et al. (2014), Richmond and Maute (2013), and related references. TIEGCM v2.0 covers altitudes ranging from approximately 97 km up to 450–600 km, with "standard" resolution set at 2.5° by 2.5° in geographic longitude and latitude, and four grid points per scale height vertically. The ionospheric electrodynamics are computed within a modified magnetic apex coordinate system (Richmond, 1995), while the solar spectral fluxes are determined by the Extreme Ultra-Violet (EUV) flux model for aeronomic calculations (EUVAC) model (Richards et al., 1994), using observed F10.7 values. Simulations are conducted with a timestep size of 30 s, and helium is considered a major species (Sutton et al., 2015). Ion convection patterns, as described by the Weimer (2005) model, are driven by 5-min Interplanetary Magnetic Field (IMF) "By" and "Bz" magnitudes, along with solar wind velocity and density. High-latitude energy input associated with auroral particle precipitation is modeled based on an analytical auroral model (Roble & Ridley, 1987).

An ICON-adapted version of TIEGCM (Maute, 2017; Maute et al., 2023), herein referred to as "TIEGCM-ICON," is employed. In this TIEGCM-ICON configuration, the model's lower boundary (LB) is specified based on ICON/MIGHTI wind and temperature measurements (L2 v05) using an Hough Mode Extension (HME) fitting method (e.g., Forbes & Hagan, 1982; Oberheide et al., 2011a, 2011b). As mentioned in Section 2.3, MIGHTI provides wind and temperature data over both day and night in the lower thermosphere (ca. 94–105 km). Over a 24-hr LST cycle of around 45 days, these wind and temperature data sample every combination of longitude and LST extending from about 10°S to 40°N latitude. These data are used to derive global fits to empirical HME functions. These fits provide an estimate of the global structure of the upward propagating diurnal and semi-diurnal tides in the lower thermosphere. Further details on the HME fits for ICON can be found in Forbes

et al. (2017) and Cullens et al. (2020). TIEGCM-ICON is based on the TIEGCM v2.0 release with descriptions of the model by Qian et al. (2014). A description of the TIEGCM-ICON and the differences to TIEGCM v2.0 is provided in Section 2.2 of Maute (2017). Tidal propagation is notably influenced by the atmospheric background; hence, employing a realistic background improves the characterization of seasonal and latitudinal variability in tidal propagation and dissipation (e.g., Jones et al., 2014). TIEGCM-ICON incorporates background climatologies from the Mass Spectrometer Incoherent Scatter Radar Extended (MSISE00) (Picone et al., 2002) and the horizontal wind model (HWM07). Based on Jones et al. (2014), no significant differences are expected by replacing HWM07 with HWM14 (Drob et al., 2015). It should be noted that, given the focus on IS time scales, no significant impacts are expected on the results contained in Section 3 from the particular background climatologies selected for running TIEGCM-ICON.

This study employs three TIEGCM-ICON simulations for analysis, all extending from December 2019 to January 2022:

- **Run 1:** HME diurnal/semidiurnal tidal forcing at the LB, realistic geophysical forcing (*"WeiHmeV2"*)
- **Run 2:** HME diurnal/semidiurnal tidal forcing at the LB, constant geophysical forcing (*"WeiHmeV2_conGeop"*)
- **Run 3:** no tidal forcing at the LB, realistic geophysical forcing (*"WeiNoHmeV2"*)

We choose the December 2019 to January 2022 period to focus on a range of consistent low-activity geomagnetic and solar conditions, which allowed us to isolate tidal effects more effectively. While data does extend through late 2022, we felt that including this period would introduce additional complexity from increased solar activity in mid-2022, which could confound the analysis of IS variability.

3. Methods

Various methodologies are used to isolate the IS variability in the TIEGCM-ICON thermospheric winds and tides, and to investigate their connections to tropospheric sources. While some analyses extend to latitudes up to ±60°, most of the focus is on equatorial regions (±15°), where the tidal coupling between the lower/middle atmosphere and the thermosphere may be expected to be the strongest (e.g., Li et al., 2024). The statistical significance of spectral peaks is established through wavelet-type analysis, a technique commonly used to analyze localized variations of power within a time series (Torrence & Compo, 1998). This approach allows the decomposition of a time series into time-frequency space, enabling the identification of dominant modes of variability and their temporal evolution. Wavelet transforms have been widely applied in geophysical studies, including those on tropical convection and thermosphere-ionosphere (T-I) interactions (Yamazaki, 2023). In this study, we use the wavelet analysis package of Torrence and Compo (1998), incorporating the rectification method of Liu et al. (2007) to enhance accuracy and reliability.

The analyses are performed on "filtered" time series to isolate IS variations in the relevant quantities within the time domain and to gain insights into their amplitudes and temporal variability. This "filtering" process involves: (a) creating residuals for each day by subtracting 90-day running means from the raw data; and (b) applying a 5-day running mean to the residuals to reduce noise. While this "filtering" is not a "true" band-pass filter, it has been successfully employed to study periodic signals in thermospheric data in the time domain (e.g., Forbes et al., 2006; Gasperini et al., 2023a, 2023b; Hughes et al., 2022). In this study, we refer to these 5-day running means of 90-day residuals as "filtered" time series. Furthermore, correlation analyses are used to identify and characterize IS variations in the thermosphere and their potential tropospheric sources. Specifically, lagged correlation analysis is performed on (a) the time series of MJO RMM1 index and thermospheric tides, and (b) the time series of thermospheric tides and the ISO amplitude of the zonal mean zonal wind. Correlation coefficients are determined using Pearson's distribution, with thermospheric oscillations treated as the dependent variable and tropospheric oscillations as the independent variable. A moving correlation coefficient, as described at the end of Section 4, is used to provide further insights. The distribution here refers to the variability within the data, which allows us to better quantify correlations between thermospheric and tropospheric oscillations. To clarify, the distribution we referred to is not a fitted statistical distribution but rather the variability within the observed data itself. This variability allows us to identify and quantify correlations between thermospheric and tropospheric oscillations across different time periods. We do not fit a separate distribution to the data but instead calculate correlation coefficients directly from the temporal variability of the oscillations. The thermospheric oscillations are treated as the dependent variable because we are primarily interested in how variability in the lower atmosphere (MJO-driven tides)

influences the thermosphere. This choice is consistent with the objective of studying the upward propagation of tidal variability.

Characterizing the complete diurnal and semidiurnal tidal spectrum necessitates resolving zonal wavenumbers and periods (e.g., Yamazaki, 2023). This analysis requires two-dimensional (2-D) spatiotemporal data, specifically data as a function of longitude and time. Techniques such as the 2-D fast Fourier transform (FFT) (e.g., Hayashi, 1971) and the 2-D least squares fitting method (e.g., Wu et al., 1995) can be employed to determine the zonal wavenumber, wave period, amplitude, and phase of a particular tidal component. Given the transient nature of tides in the lower thermosphere, a short-time analysis is typically used. In this study, for tidal analysis of the TIEGCM-ICON model output, we apply the 2D (space-time) FFT on a daily basis, progressing one day at a time. The spectral decomposition technique of Hayashi (1971) is used to resolve westward or eastward propagating waves. The Hayashi (1971) method is straightforward to implement, and its spectrum directly provides wave amplitudes in units of the input data, facilitating interpretation. It is important to note that while the TIEGCM-ICON LB tides are derived using 45-day means of ICON MIGHTI observations, the effects of dissipation and mean winds above the LB, nonlinear interactions, and in situ wave generation can cause significant day-to-day variability in the thermospheric tidal spectrum. Thus, TIEGCM tidal amplitudes and phases are obtained on a daily basis using the technique discussed above.

Additionally, to examine the connection between the MJO and tidal variations, we employ a standard MJO diagnostic known as Hovmöller analysis (Wheeler & Kiladis, 1999), following an approach similar to Kumari et al. (2021). The Hovmöller analysis involves: (a) applying a 30–90 days bandpass filter on tidal amplitudes and phases and (b) extracting the eastward-propagating signal. Unlike previous studies (e.g., Gasperini et al., 2020; Kumari et al., 2020; Yang et al., 2018), which focused solely on tidal amplitudes, the analysis incorporates tidal phase values into the Hovmöller analysis of tidal perturbations. As noted by Kumari et al. (2021), this bandpass filtering reduces noise errors in the input data thus resulting in a "cleaner" MJO signature. Note that the 5-90-day band-pass filter is chosen to capture a broad range of IS variability, allowing us to observe periods relevant to both the MJO and other IS phenomena. This filtering helps distinguish the 27-day solar rotation effects in geophysical indices from the IS variability associated with the MJO index. For the Hovmöller analysis, we use a narrower 30–90 days band-pass to focus specifically on the eastward-propagating IS variability related to the MJO, which aligns with its dominant timescales. This approach is a methodological choice to emphasize distinct temporal features in each analysis, not a limitation from SABER.

4. Results

The focus of this study is on the period spanning from 1 January 2020 to 31 December 2021, characterized by low geomagnetic and solar activity influences. Initially, we assess the geophysical conditions specific to this timeframe. Figure 1 includes time series plots of daily Kp geomagnetic and F10.7 solar radio flux indices (black lines), alongside their filtered counterparts (blue lines) and wavelet analyses of their daily filtered values. Daily Kp values consistently remain below 3.0, indicative of (relatively) low geomagnetic activity conditions. The F10.7 solar flux shows variability within the range of 75 SFU to 125 SFU, typical for solar minimum to medium conditions. Filtered Kp (F10.7) values range from −1 (−20 SFU) to +2 (+20 SFU). Wavelet analyses of Kp and F10.7 reveal pronounced variations with periods close to the solar rotation period of ∼27 days, particularly notable during September-December 2020 and July-December 2021, as corroborated by the filtered time series. Additionally, Figure 1 depicts the time series of OLR and RMM1 indices (black lines), along with their filtered time series (blue lines) and wavelets. In contrast to the geomagnetic and solar indices, which exhibit significant variations in the 20–40 days range, OLR and RMM1 demonstrate prominent IS variations spanning periods from 40 to 120 days throughout the two years. These IS variations in RMM1 will be further analyzed in subsequent sections of this study.

Next, we analyze the near-equatorial (±15° average) zonal- and diurnal-mean (i.e., longitudinal and 24-hr UT/LT averaged, hereafter "ZDM") zonal winds at ∼150 km (pressure level 20) and ∼300 km (pressure level 40) altitudes for the three TIEGCM-ICON cases listed in Section 2.5: ("Run 1") TIEGCM with HME tidal forcing at the LB and realistic geophysical forcing ("WeiHmeV2"), ("Run 2") TIEGCM with HME tidal forcing at the LB but constant geophysical forcing ("WeiHmeV2_conGeop"), and ("Run 3") TIEGCM with no tidal forcing at the LB but with realistic geophysical forcing ("WeiWoHmeV2r1"). Geophysical forcing for "Run 2" is: F10.7 = 71 sfu, solar wind speed = 400 km/s; solar wind density = 4.1/cm^3, IMF By = 0 nt, Bz = 1 nT, hemispheric

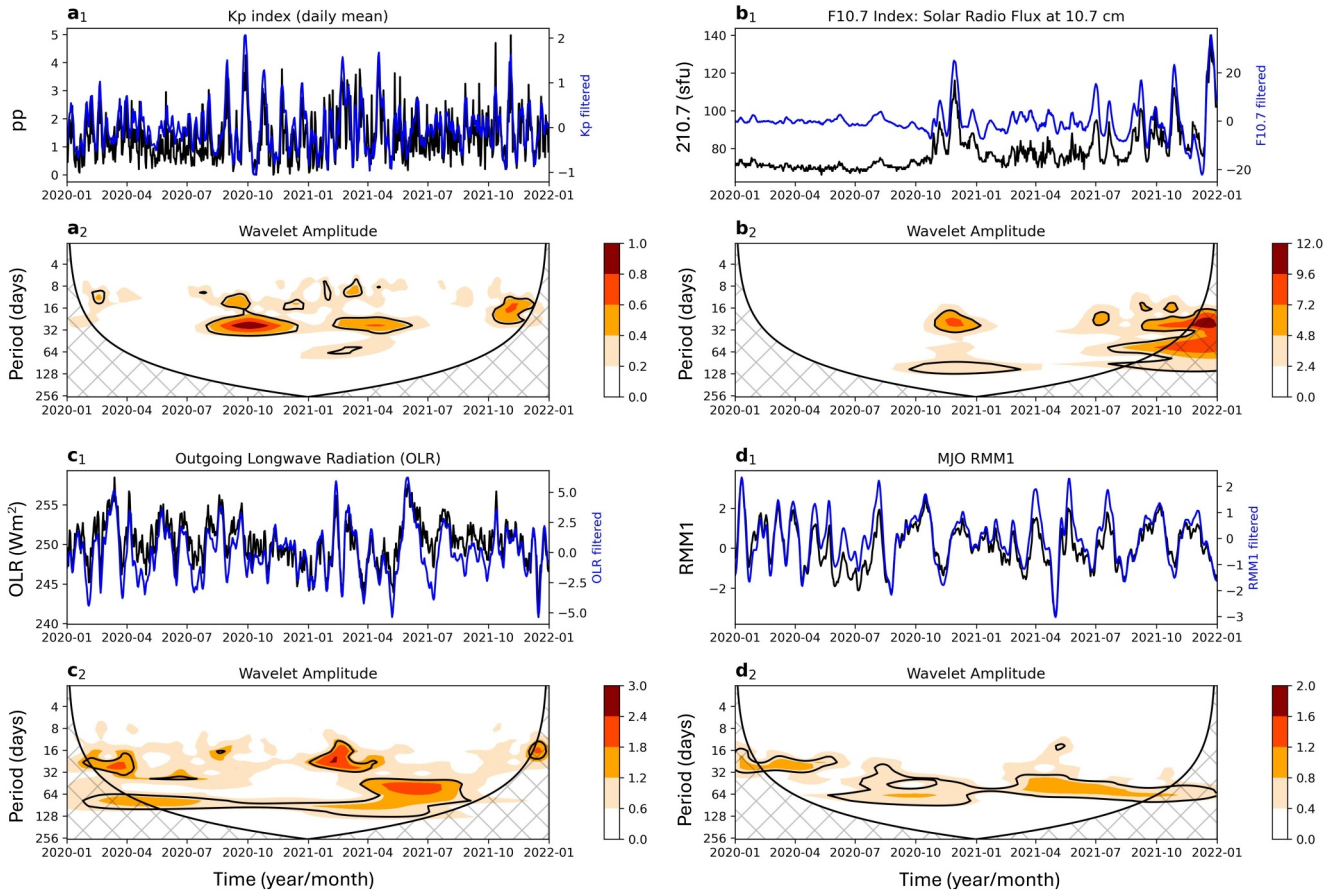

Figure 1. Time series of daily Kp and F10.7 values (panels a_1 and b_1) before (black lines) and after (blue lines) a 5–90-day filter is applied. The respective Morlet wavelets are shown in panels a_2 and b_2. Similarly, time series (wavelets) of equatorial (±15° latitude mean) Outgoing Longwave Radiation and RMM1 amplitudes are shown in panels c_1 and d_1 (c_2 and d_2), respectively.

power = 12 GW. The time series of ZDM zonal winds at ~150 km altitude for "Run 1," "Run 2," and "Run 3" are depicted in Figures 2a1–2c1, respectively, showing daily values (black lines) and filtered values (blue lines), while their corresponding Morelet wavelets are presented in Figures 2a2–2c2. For "Run 1," the time series and wavelets reveal significant IS variability of about ±15 m/s over the span of 2 years, exhibiting a particularly pronounced periodicity of around 64 days. This periodic behavior in the ZDM zonal winds, peaking notably around October-December 2020 and July-November 2021, mirrors similar periodicities observed in RMM1 and partly ORL (ref. Figures 1c2 and 1d2). Note that while the peak in ZDM zonal winds occurs around October-December OLR does not show this same behavior.

The differences observed during the equinox transitions within each year reflect intra-annual variations, rather than inter-annual changes. These variations highlight the dynamic nature of the coupling between the lower and upper atmosphere during the equinox periods. While both phenomena can impact atmospheric dynamics, the MJO's influence is related to its IS variability and the propagation of its associated atmospheric waves. In contrast, the differences between years of equinox transition are mainly driven by annual changes in solar radiation and the resulting variations in atmospheric circulation patterns. Therefore, these influences are not the same but may interact in complex ways to affect thermospheric conditions. Additionally, variations of about ±5 m/s occurring near 27 days (and its harmonics at ~13.5 days and ~54 days), evident during August 2020, April-May 2021, and October-November 2021, are closely aligned with variations in the geomagnetic (Figure 1a2) and solar (Figure 1b2) indices. These fluctuations are attributed to the well-documented influence of solar rotation variation in EUV flux on thermospheric parameters (e.g., Qian & Solomon, 2012 and references therein). In contrast, "Run 2" displays substantial IS variability akin to "Run 1," but lacks the characteristic variability around 27 days

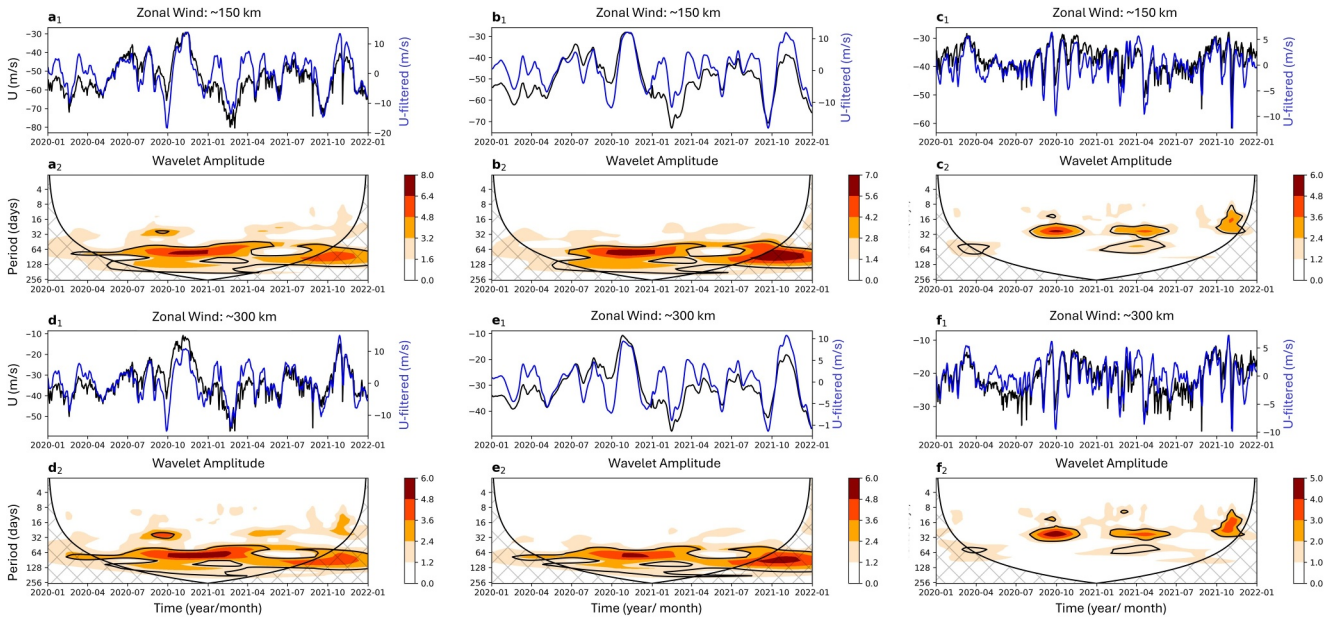

Figure 2. Time series of zonal and diurnal mean zonal winds near the equator (±15° latitude mean) and 150 km altitude for TIEGCM-ICON "Run 1" (i.e., "WeiHmeV2") (panel a_1), "Run 2" (i.e., WeiHmeV2_conGeop) (panel b_1), and "Run 3" (i.e., WeiWoHmeV2) (panel c_1). The corresponding Morlet wavelets are shown in panels a_2–c_2 respectively. Panels d_1–f_1 (d_2–f_2) are similar to panels a_1–c_1 (a_2–b_2) but near 300 km altitude.

associated with solar and geomagnetic activity as geophysical forcing is kept constant for this case. Similarly, a direct comparison of unfiltered ZDM zonal wind time series between "Run 1" and "Run 2" clearly highlights shorter-term (∼ 5-30-day) solar/geomagnetic-induced variations in "Run 1," absent in "Run 2." The observed differences are anticipated, considering the lack of variability in external geophysical forcing for 'Run 2'.

A compelling result is obtained from the analysis of "Run 3." The time series (Figure 2c1) and wavelet (Figure 2c2) of "Run 3" reveal solar/geomagnetic-induced variations around 27 days and their harmonics, but lack any IS variations in the 60–100 days range, notably the ∼64-day variation observed in both "Run 1" and "Run 2." This finding indicates that the ±15 m/s variability in ZDM zonal winds around 150 km in "Run 1" and "Run 2" is largely driven by the diurnal and semidiurnal tides propagating from below ∼97 km. Although these results specifically address the 150 km altitude region, similar conclusions apply to higher altitudes, such as near 300 km, as illustrated in Figures 2d1–2f1 and 2d2–2f2. In Figure 2, different scales are used for the three model simulations to emphasize the distinct amplitude variations in each case. For detailed comparisons of the amplitudes with consistent scales, please refer to the follow-on figures provided later in this manuscript. Detailed analyses of latitudinal and altitudinal dependencies in the IS response of ZDM winds to the upward propagating tidal spectrum are provided in subsequent sections.

The results presented in Figure 2 demonstrated that the diurnal/semidiurnal tidal spectrum entering the lower thermosphere near 97 km is a leading driver of the dynamical variability in the mean thermospheric zonal winds around IS time scales. Comparable results have been observed for other model parameters, such as thermospheric temperature, composition, and density. It is likely that ionospheric quantities, including electron density, ion drifts, and total electron content, will exhibit similar effects, which will be investigated in a dedicated follow-up study. Next, we aim to characterize the altitude, latitude, and month-of-year (moy) dependencies on this tidal-induced IS variability in ZDM zonal winds. To this end, we compute difference fields between the full model outputs from "Run 1" (with ICON/HME tides at the LB) and "Run 3" (with no tides at the LB). Note that both "Run 1" and "Run 3" incorporate the same geophysical forcing, hence the difference fields are expected to exhibit negligible variability associated with "external" forcing and thus enable us to focus on the thermospheric effects from the LB tides.

Next, we examine the altitude-moy contours of the ZDM zonal winds near the equator (±15°) from "Run 1" (Figure 3a1) and the "Run 1" - "Run 3" difference field (Figure 3a2), along with the 5-90-day-filtered variations

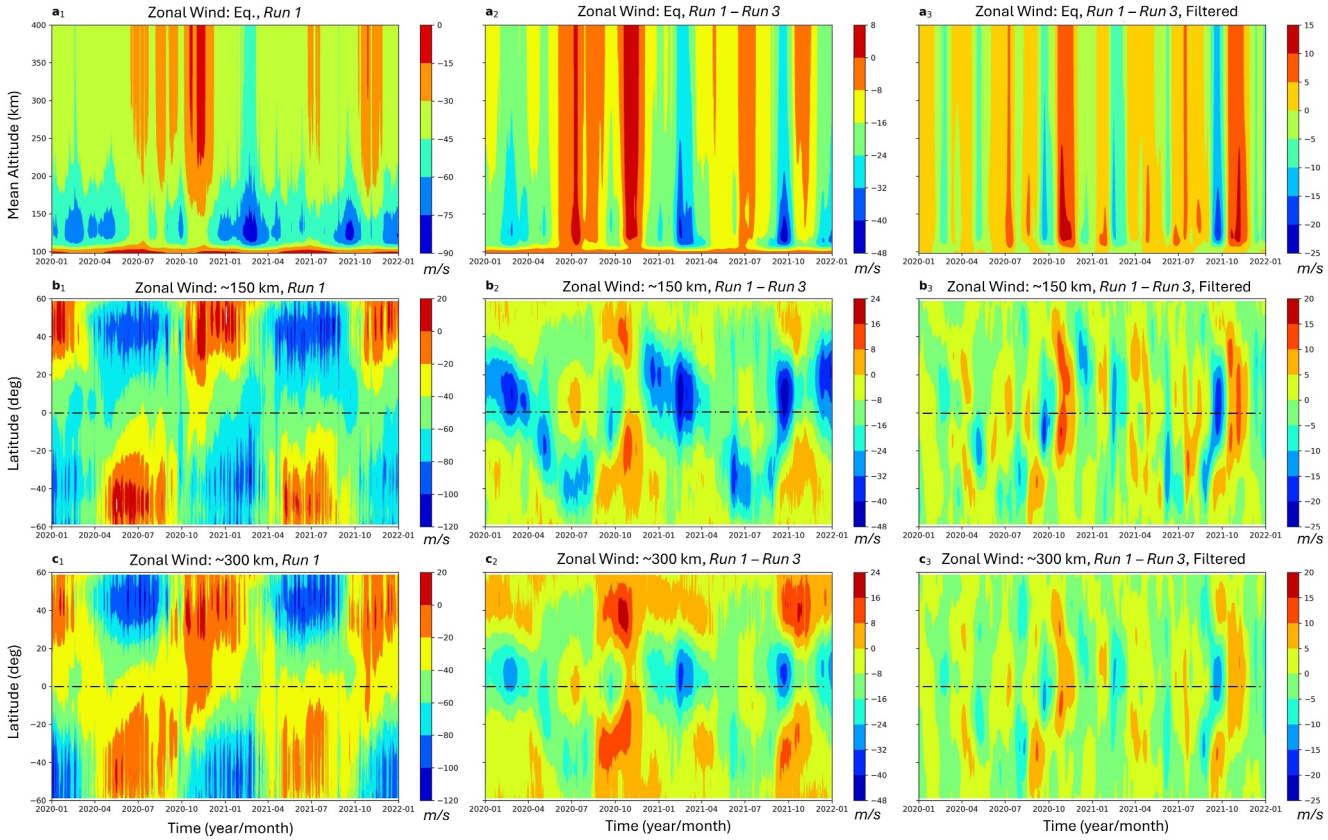

Figure 3. (a_1) Altitude (~100–400 km) versus time (month-of-year, moy, since January 2020) contours of TIEGCM-ICON zonal and diurnal mean zonal wind (m/s) near the equator (±15°latitude mean) from "Run 1." (a_2) Same as (a_1), but as the difference between "Run 1" and "Run 3." (a_3) Same as (a_2), but after the 5–90-day filter is applied. (b_1)–(b_3) Same as (a_1)–(a_3), but as latitude (60°S–60°N) versus moy contours near 150 km altitude. (c_1)-(c_3) Same as (b_1)-(b_3), but near 300 km altitude.

of the difference field (panel a_3). Consistently with the wavelet results in Figure 2, the IS variations in ZDM zonal winds maximize around October-December 2020 and July-November 2021 with variability up to ± 20 m/s. The altitude-moy structure of the filtered ZDM winds is in general agreement with previous modeling results by Gasperini et al. (2017a) who examined a MERRA-2-forced TIMEGCM simulation and satellite observation during 2009–2010 demonstrating a connection between the background zonal winds, the DE3 tide, and tropical tropospheric convection. Using only a model simulation with realistic LB and external forcing, Gasperini et al. (2017a) could not unequivocally determine and quantify the sources of IS variations in the mean winds and the associated dependencies on altitude and latitude. As shown in Figure 3a3, the tidally induced zonal wind ISOs maximize in the lower thermosphere near 110–130 km altitude. This region is where upward-propagating tidal components undergo significant dissipation imparting their energy, momentum, and temporal variability to the background (e.g., Truskowski et al., 2014). Remarkably, and in agreement with Gasperini et al. (2017a), the tidally driven mean wind ISOs retain significant values even in the middle and upper thermosphere with variations exceeding ±15 m/s near 400 km altitude.

Proceeding further, we investigate the tidally induced latitude-moy structure in the ZDM zonal winds around two altitudes of interest: 150 km (Figures 3b1–3b3) and 300 km (Figures 3c1–3c3). For both altitudes, the IS variability is shown to be most prominent within about ±20° latitude (ref. Figures 3b3–3c3) and display values up to about ±20 m/s (±15) near 150 km (300 km). Notably, the latitude structure of the ISOs is strongly time-dependent. A closer examination of Figures 3a3 and 3b3 reveals dominant equatorially symmetric and asymmetric latitude structures that vary in importance through the 2 years. This result points to the collective effect of multiple tidal components in determining the latitude-moy-altitude structure of the background zonal wind. Each tidal component has its dominant Hough modes, with the amplitude of each Hough mode strongly dependent on latitude and season (e.g., Forbes et al., 2022; Gasperini & Oberheide, 2024; Oberheide et al., 2011a, 2011b). The

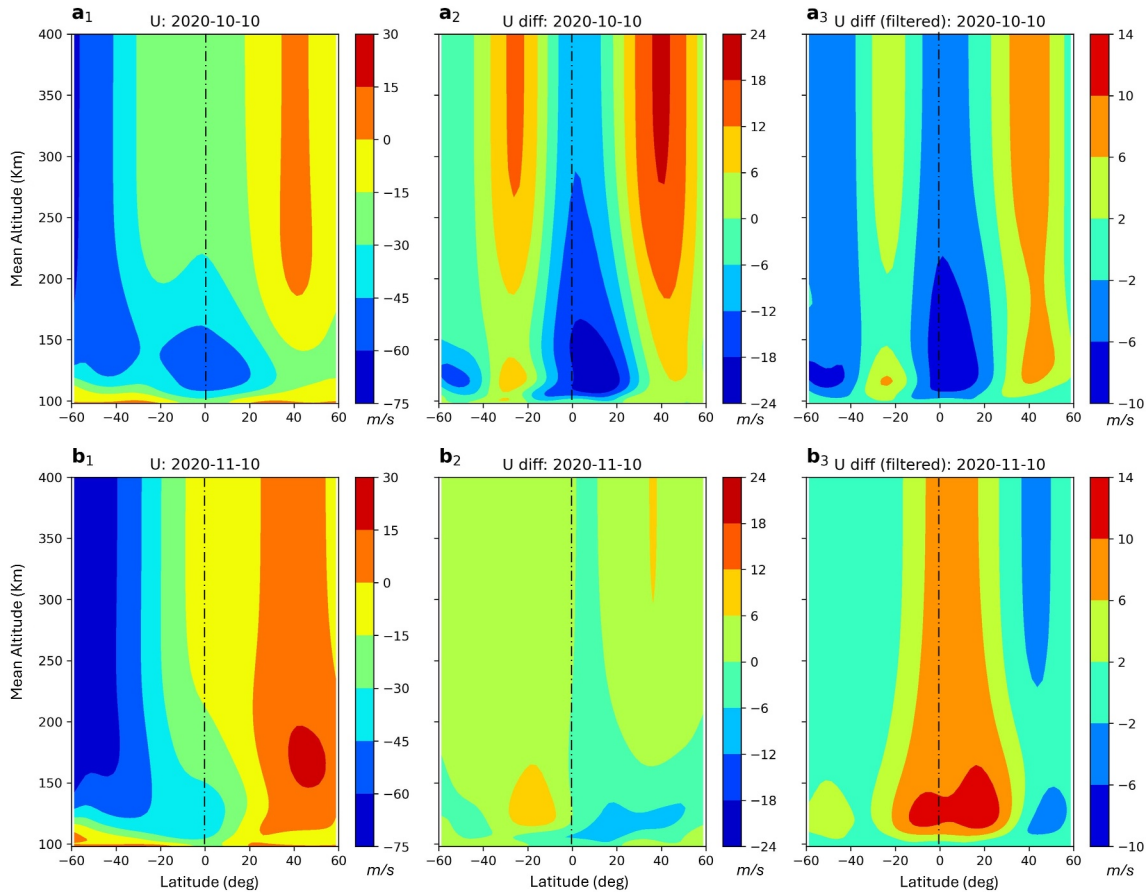

Figure 4. Altitude (~100–400 km) versus latitude (60°S–60°N) contours of zonal and diurnal mean zonal winds centered on 10 October 2020 for Thermosphere Ionosphere Electrodynamics General Circulation Model "Run 1" (a_1), "Run 1" –"Run 3" (a_2), and filtered "Run 1" –"Run 3" (a_3). (b_1)–(b_3) Same as (a_1)–(a_3), but centered on 10 November 2020.

effect of different tidal components on the observed zonal wind ISOs is examined in further detail in the later part of this study. Note that due to the ~45-day averaging associated with the MIGHTI/HME fitting, tidally driven ZDM zonal winds exhibit no appreciable variability with periods shorter than ~30 days. Consequently, it is deemed appropriate to employ 5–90 days "filtered" fields (as detailed in Section 3) to quantify "IS variability."

Figure 4 investigates the altitude-latitude structure of IS variations induced by tides in the ZDM zonal winds, focusing on two specific days with significant and oppositely phased IS variations: 10 October 2020 (Figures 1a1) and 10 November 2020 (Figures 1b1–1b2). Figures 4a2 and 4b2 show the ZDM zonal winds derived from the difference field between "Run 1" and "Run 3." The middle panels (a_2, b_2) represent this difference field, while the right panels (a_3, b_3) display the filtered difference field to highlight the IS variations. The left panels (a_1, b_1) show the unmodified zonal winds from "Run 1" for comparison. Furthermore, filtering is applied to this mean zonal wind field to highlight IS variations. The IS variability is found to be in the ±10–15 m/s range, with increased westward (eastward) ZDM zonal winds between approximately 10°S−20°N and 60°S−40°S (40°S−10°S and 20°N−60°N) on 10 October. A nearly opposite latitudinal response is observed on 10 November, with increased eastward winds around ±20−30°S latitude and westward wind enhancements generally present at mid-latitudes.

The latitudinal structures appear more pronounced in the filtered data, while the unfiltered data lacks this clarity due to the influence of broader-scale variability (as highlighted by the respective color bar scales). A more detailed visual inspection of Figure 4 reveals significant latitudinal asymmetries in the background zonal wind response to the upward propagating tidal spectrum. The winds exhibit a latitudinal shift, with the patterns shifted toward the northern hemisphere by about 10° on 10 October. In contrast, on 10 November, the patterns are shifted toward the southern hemisphere by a similar extent, likely due to the influence of mean wind and its interaction

with upward-propagating tidal modes. Vertically varying mean winds can effectively alter the altitude-latitude propagation characteristics of different tidal modes, strongly depending on the longitudinal direction of propagation, frequency, and wavenumber. More discussion on this topic is provided below as the latitude-moy structure and IS variability of different tidal components are examined. Finally, as best exemplified in Figures 4a3 and 4b3, it is important to note that the altitude of maximum background wind variations occurs around 100–130 km, the altitude region where the upward-propagating tidal spectrum capable of reaching the lower thermosphere undergoes the most significant dissipation. Variability in the dominant tidal components is likely to be a leading source of difference in the altitude-latitude structures between the 2 days.

The ICON-HME-informed TIEGCM simulations have thus far demonstrated the prominent role of the lower thermospheric diurnal and semi-diurnal tidal spectrum in generating IS variability in the ~100–400 km altitude region, with the strongest effects on the background zonal wind occurring at low latitudes and around 110–130 km altitude. Next, to gain better insights into the role played by the upward-propagating tidal spectrum we analyze the altitude-moy and latitude-moy structures of the nonmigrating DE2 and DE3 tides and the migrating DW1 and SW2 tides. It is important to note that, aside from DE2 and DE3, other upward-propagating tidal components from the lower/middle atmosphere can play an important role in the whole-atmosphere coupling on IS timescales (notably SE2 and DE1). However, it would be beyond the scope of this paper to examine all the tidal components from these model simulations in detail and this effort is left for follow-on work that may need to account also for terdiurnal tides and ultra-fast Kelvin waves (not included in the TIEGCM LB). The vertical structure of zonal wind DE2, DE3, DW1, and SW2 amplitudes as a function of time (2020–2021) between 100 and 400 km from TIEGCM-ICON "Run 1" are contained in Figures 5a1–5d1, respectively. Figures 5a1–5d1 present the unfiltered tidal amplitudes, while Figures 5a2–5d2 display the same components after the application of a 5-90-day filter to highlight IS variability. From these depictions, it is clear that the amplitudes of the nonmigrating DE2 and DE3 tides grow exponentially with height up to ~120 km, the altitude region where dissipation stops their growth causing the amplitudes to decrease before reaching asymptotic values above about 200 km altitude. Molecular diffusion is the dominant dissipation mechanism for vertically propagating waves in the thermosphere.

As established by Chapman and Lindzen (1970), the exponential growth of an upward-propagating tide ceases in altitude regions where the timescale for molecular dissipation approximates the wave period ($\chi \sim 1$). In this context, χ is defined as $\chi = \left|\frac{2\pi}{\lambda_z^2}\frac{\mu_0}{\rho}\frac{1}{\sigma}\right|$, where λ_z represents the vertical wavelength, μ_0 denotes the molecular dissipation coefficient, ρ is the mean density, and σ stands for the wave frequency. When $\chi \sim 1$, molecular processes dominate, and a tide shifts from exponential growth to decay. The altitude where $\chi \sim 1$ depends quadratically on λ_z^2, and also varies with the wave frequency σ and mean density ρ. The first symmetric Hough modes of DE2 and DE3 encounter $\chi \sim 1$ in the altitude range of approximately 110–130 km, corresponding to peaks in amplitude as shown in Figures 5a1–5b1. As previously mentioned, classical tidal Hough functions serve as the orthogonal bases for the latitudinal structure of tidal components, while HMEs represent the altitude extension of these Hough functions incorporating tidal dissipation mechanisms. Tides can be expressed as a combination of HMEs. The primary characteristics of the DE3 in the mesosphere-lower thermosphere (MLT) can be effectively captured by a combination of the first symmetric mode (equatorial, HME1) and the first anti-symmetric mode (non-equatorial, HME2), whereas DW1 is predominantly composed of the first symmetric component (HME1).

As a major driver of IS variability in the thermosphere, DE3 originates primarily from latent heat release in deep convective clouds in the tropical troposphere (e.g., Hagan & Forbes, 2002; Hagan et al., 2007; Oberheide et al., 2011a, 2011b). DE3 shows peak amplitudes around 15 m/s in zonal winds near 95 km (e.g., Forbes et al., 2003; Talaat & Lieberman, 1999) and upward of 20 m/s near 260 km (e.g., Gasperini et al., 2015, 2020). The symmetric mode HME1 of DE3, characterized by λ_z of ~56 km, extends higher into the thermosphere and peaks typically from July to November (e.g., Forbes et al., 2022; Gasperini et al., 2023a, 2023c; Gasperini & Oberheide, 2024; Oberheide et al., 2011a, 2011b). This enhanced forcing is driven by a combination of factors. As demonstrated by Zhang et al. (2012), the seasonal-latitudinal variation of the DE3 tide is modulated by both the distribution of tidal heating in the troposphere (from radiative and latent heating) and the background zonal wind. The mean zonal wind can filter and modulate the upward propagation of DE3 tidal energy, altering its seasonal and latitudinal distribution in the MLT region. These processes collectively contribute to the stronger DE3 amplitudes observed during this period.

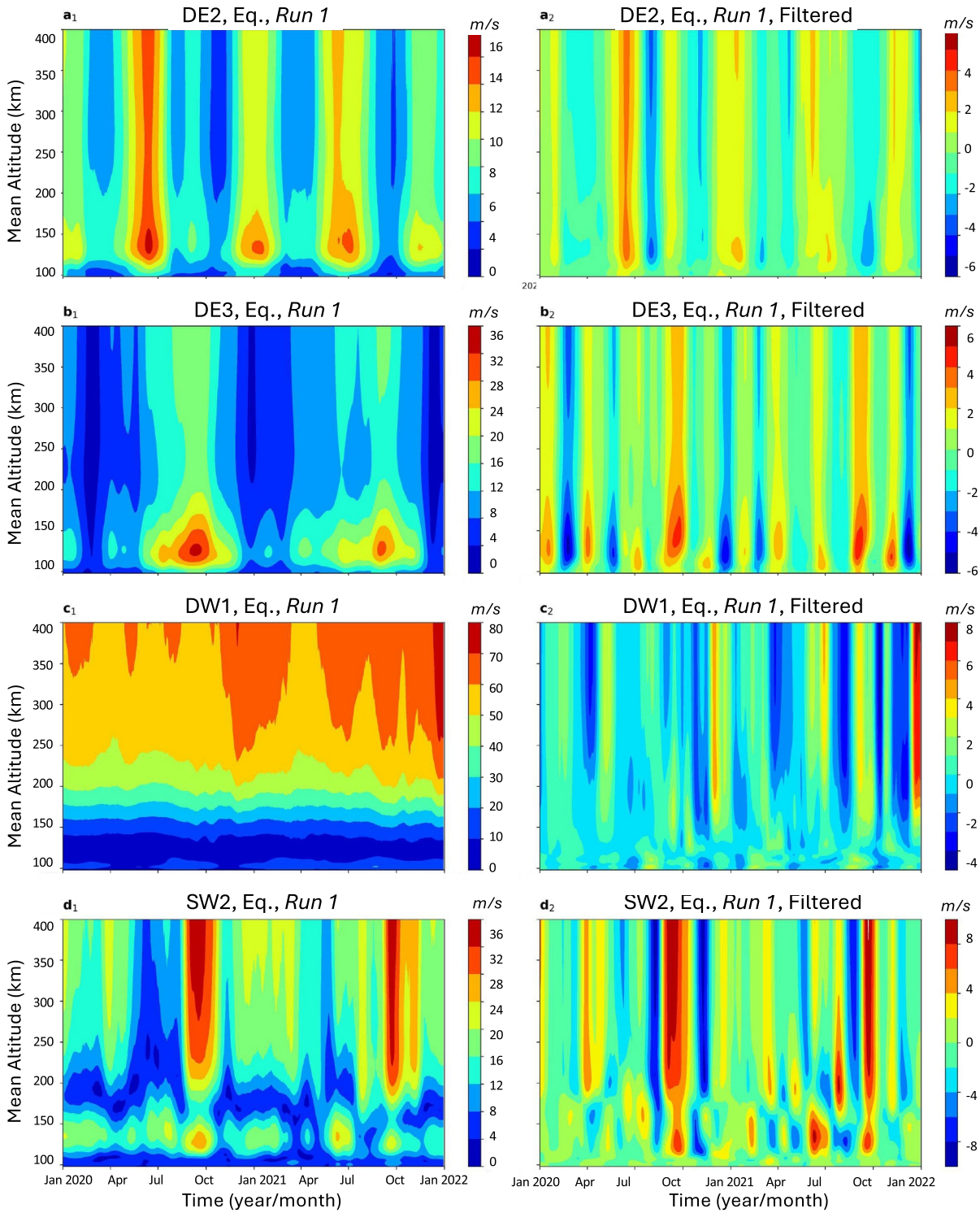

Figure 5. TIEGCM-ICON "Run 1" zonal wind DE2 (panel a_1), DE3 (panel b_1), DW1 (panel c_1), and SW2 (panel d_1) amplitudes near the equator (15°S−15°N mean) as a function of altitude (~100–400 km) and time (months since January 2020). Panels a_2–d_2 show the tidal amplitudes of DE2, DE3, DW1, and SW2, respectively, after a 5–90-day filter is applied.

Conversely, the antisymmetric mode HME2 of DE3, with $\lambda_z \sim 30$ km, shows increased amplitudes, dominating the DE3 spectrum from December to February. Mean wind fields are known to significantly distort the altitude-latitude tidal structures between 100 and 400 km (Gasperini et al., 2017b). The asymmetries in DE3 and other upward-propagating tidal components primarily arise from the linear superposition of one or more antisymmetric modes, generated through processes such as "mode coupling" (e.g., Lindzen & Hong, 1974) or "cross-coupling" (e.g., Walterscheid & Venkateswaran, 1979a, 1979b). Mean winds primarily distort the height-latitude structures of eastward propagating waves, like DE3 and DE2, by aligning them with westward wind regimes in the thermosphere. Theoretical interpretations (e.g., Forbes, 2000; Forbes & Vincent, 1989; Gasperini et al., 2017b) suggest that westward (eastward) zonal mean winds Doppler-shift eastward propagating waves to higher (lower) frequencies and longer (shorter) vertical wavelengths, thus reducing (increasing) their dissipation effects.

The unfiltered DE2 (Figure 5a1) shows prominent maxima below 200 km and considerable amplitudes extending up to 300 km, with clear periodic enhancements occurring approximately every 6 months. The filtered DE2 amplitudes (Figure 5a2) highlight large IS variations, with the most significant activity around 100–150 km and recurring peaks indicating variability in the range of 2–3 months. The DE3 tidal component (Figure 5b1) displays strong seasonal maxima around 150 km, with amplitudes decreasing with altitude. The filtered DE3 (Figure 5b2) reveals pronounced IS variability, particularly notable around 100–150 km, exhibiting periodic fluctuations over ∼60–90 days. The DW1 component (Figure 5c1) exhibits comparatively much smaller IS amplitudes of around ±6 m/s (vs. ∼80 m/s maximum amplitudes), likely due to the upward-propagating component and nonlinear wave-wave interactions. The unfiltered SW2 (Figure 5d1) shows distinct seasonal peaks around 150 km, with amplitudes extending above 200 km. The filtered SW2 (Figure 5d2) demonstrates IS variability predominantly below 200 km, with a noticeable periodicity of around 2–3 months.

Next, the latitude-temporal structure and IS variability of DE2, DE3, DW1, and SW2 tidal components in the TIEGCM-ICON model "Run 1" at an altitude near 100 km are examined. Figures 6a1–6d1 present the unfiltered tidal amplitudes, while Figures 6a2–6d2 show the same components after applying a 5-90-day filter to emphasize IS variability. The unfiltered DE2 (Figure 6a1) shows significant amplitude maxima primarily concentrated around 20°S and 20°N, with periodic enhancements over time. The filtered DE2 (Figure 6a2) reveals that IS variability occurs across all latitudes, with pronounced peaks of around reaching 3 m/s (−2 m/s) at equatorial and low-latitudes (<30°) recurring every ∼45–90 days. The DE3 component (Figure 6b1) exhibits strong amplitudes centered around the equator and extending to about 30° in both hemispheres. The filtered DE3 (Figure 6b2) highlights the IS variations of around 4 m/s, showing more localized and periodic enhancements, especially near the equator and low-latitudes (<30°), on a 2–3 months timescale. The unfiltered DW1 (Figure 6c1) has substantial amplitudes extending across a wide latitudinal range, with maxima of around 4 m/s near mid-latitudes (±30°). Filtering (Figure 6c2) reveals IS variability in DW1 with shorter periodicities (compared to DE2 and DE3) of around ∼30–60 days, visible across a broad latitudinal range but most pronounced near mid-latitudes. The SW2 component (Figure 6d1) displays distinct seasonal peaks at mid/higher latitudes (±40-60°). The filtered SW2 (Figure 6d2) shows near to no IS variability near the equator and low latitudes (<30°), with larger amplitudes up to ∼16 m/s occurring above 45° latitude and periodic peaks occurring every ∼30–60 days.

Figures 7 and 8 present the same results as Figure 6, but at higher altitudes, specifically near 150 and 300 km, respectively. The latitude structure of DE2 and DE3 undergoes significant broadening due to the effect of molecular dissipation. For example, while DE3 zonal wind amplitudes of approximately 20 m/s are confined to around ±15° latitude at around 100 km altitude (Figure 6b1), these 20 m/s DE3 zonal winds extend to latitudes as high as around 40° near 300 km (Figure 8b1). The IS variations in both DE2 and DE3 demonstrate comparable magnitudes of around 4.5 m/s across all altitudes, suggesting that the source of these variations likely originates below 100 km, as no significant in situ generation of IS variability is observed. Similar observations can be made regarding the temporal variability in the filtered amplitudes for DE2 and DE3. In Figure 6b1, the DE3 amplitude is more centered over the Southern hemisphere at 100 km, while in Figure 8b1, it is more centered over the northern hemisphere at 300 km. This latitude shift is an important observation that reflects the upward propagation of tides, which can shift with altitude due to mean winds (e.g., Gasperini, Forbes, & Hagan, 2017a). Meanwhile, DW1 and SW2 show considerably increased amplitudes above approximately 130–150 km, as also illustrated in Figures 5c1–5d1, due to the in situ generation of these migrating tidal components. Interestingly, SW2 zonal

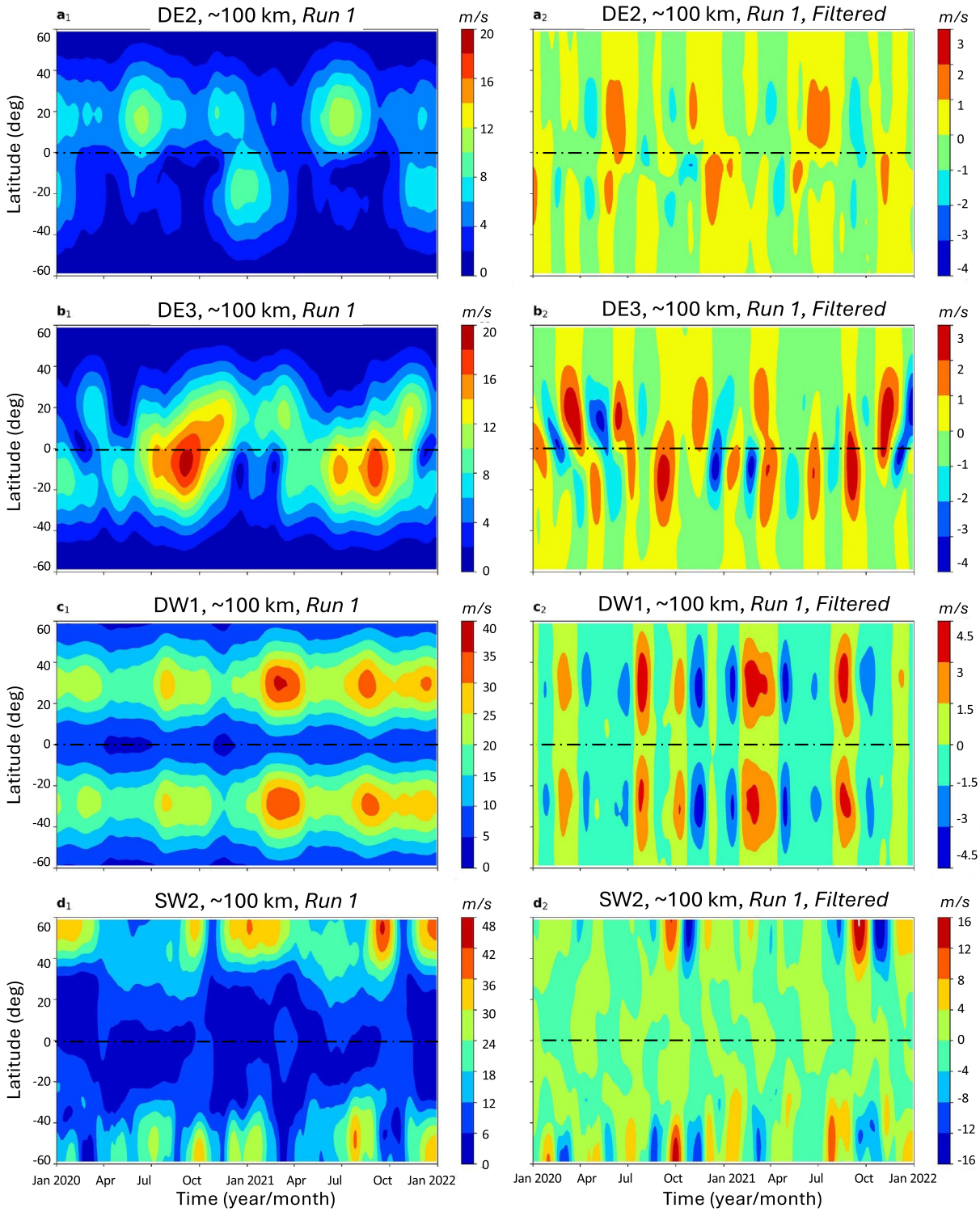

Figure 6. Latitude (60°S–60°N) versus time (months since January 2020) contours of TIEGCM-ICON "Run 1" zonal wind DE2 (panel a_1), DE3 (panel a_2), DW1 (panel a_3), and SW2 (panel a_4) amplitudes near 100 km altitude. (a_2)–(d_2) Same as a_1)–(d_1), but with a 5-90-day filter applied.

winds (Figures 5d1, 7d1, and 8d1) display substantial lower thermospheric amplitudes (~25 m/s) during August-September 2020, which are retained in the middle thermosphere. Their filtered amplitudes (Figures 5d2, 7d2, and 8d2) also exhibit prominent amplitude and vertically coherent IS variability at all altitudes during this period. This

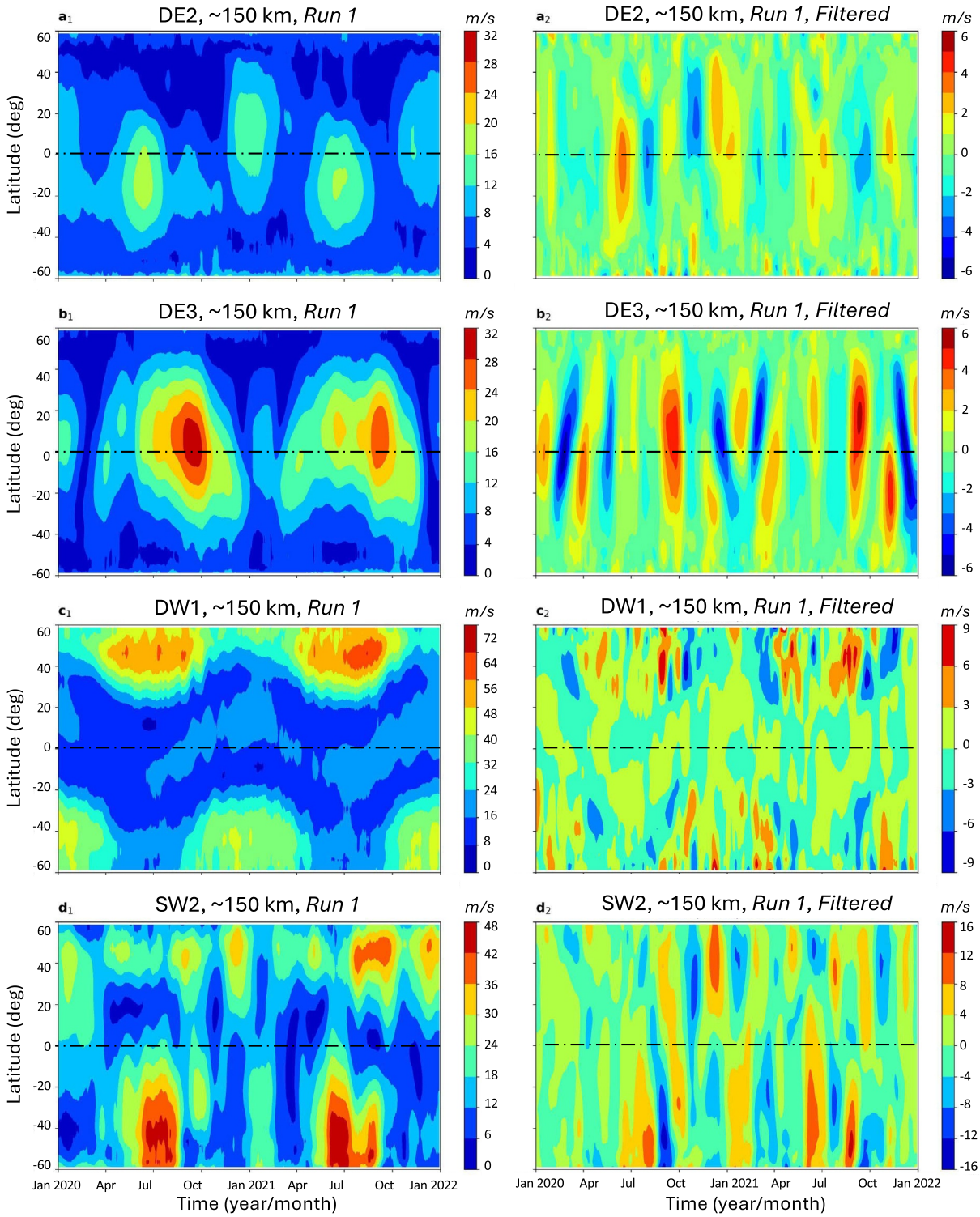

Figure 7. Same as Figure 6, but near 150 km altitude.

finding aligns with the results of Maute et al. (2023), who observed large upward-propagating SW2 in TIEGCM-ICON during the 50-day period from 7 August 2020 to 27 September 2020. Maute et al. (2023) reported significant effects of sudden changes in SW2 on the upper thermosphere and ionosphere around/after 19 August

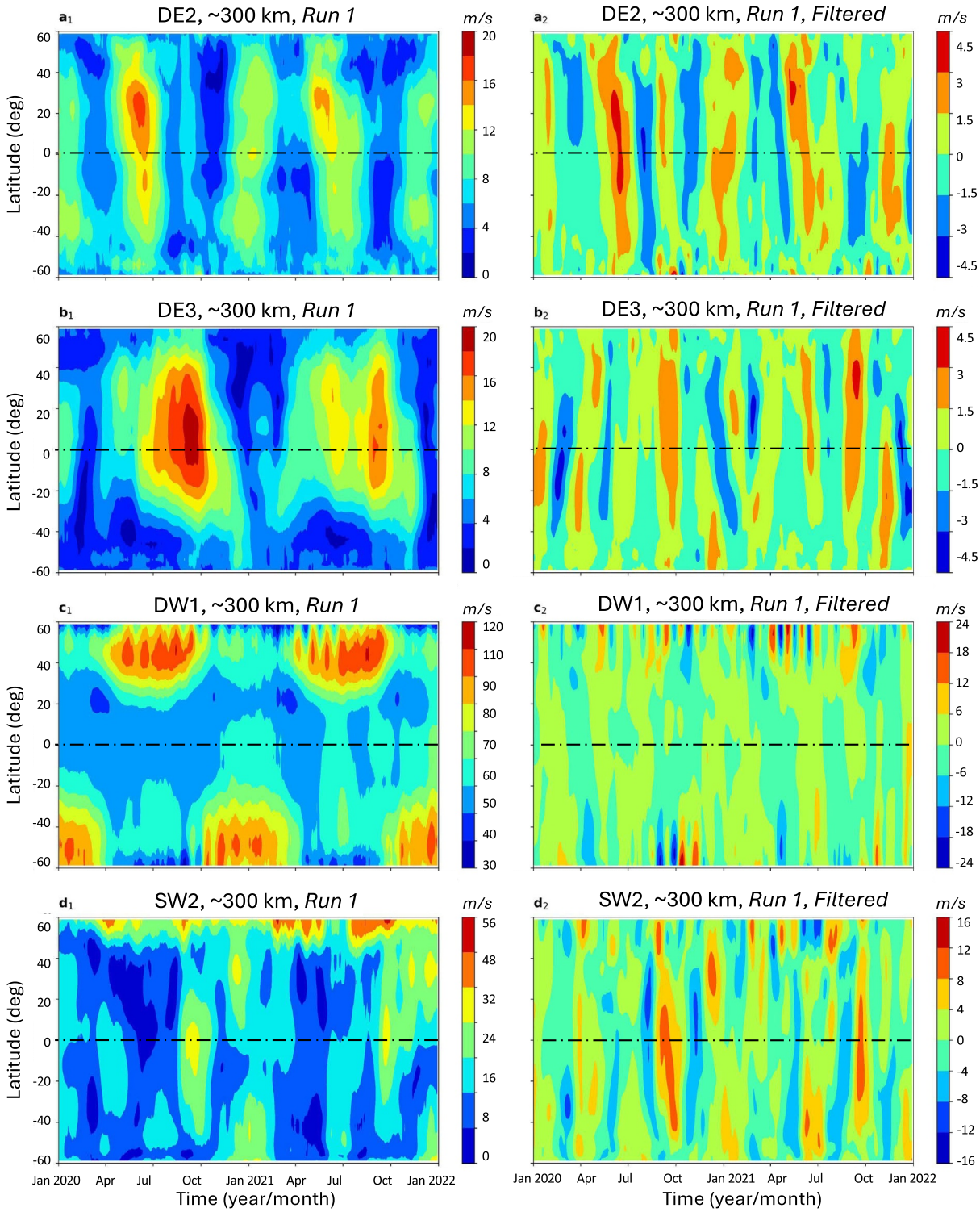

Figure 8. Same as Figure 6, but near 300 km altitude.

2020. These changes in SW2 are linked to the dominance of antisymmetric higher-mode HMEs post-August 2020 and are evident in Figure 5d1. This drastic transition can be attributed to possible influences around the equinox, associated with the combined effects of transition characteristics in different altitude regions.

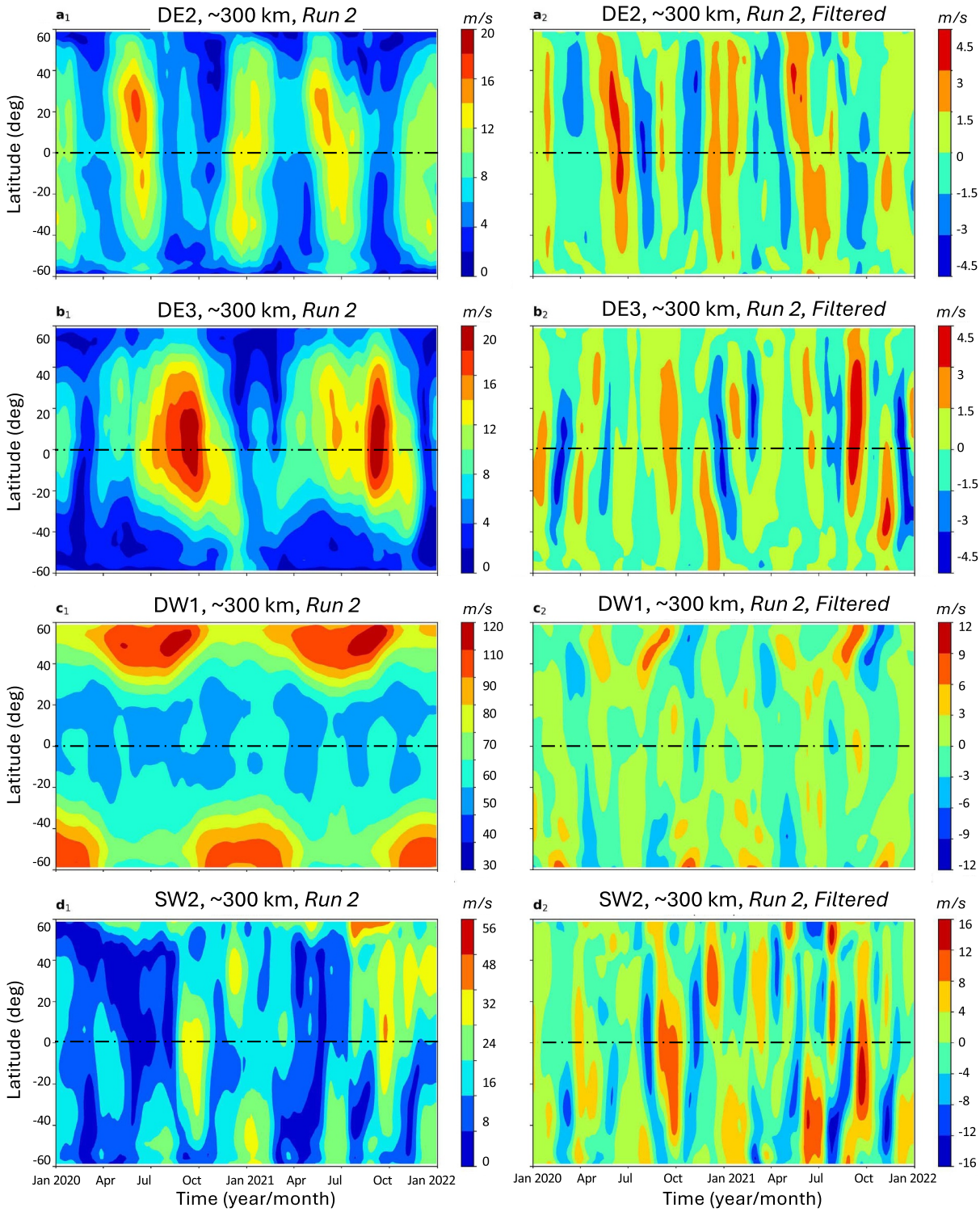

Figure 9. Same as Figure 8, but for the TIEGCM-ICON "Run 2" with constant geophysical forcing.

Figure 8 demonstrates notable ~10– to ~30-day variability in DW1 (and to a lesser extent in SW2) near 300 km, particularly at higher (>45°) latitudes. This periodic behavior in the migrating tides is attributable to geophysical forcing, particularly heating linked with the in situ generation of these two migrating tidal components in the middle thermosphere. Figure 9 illustrates the latitude-temporal structure of DE2, DE3, DW1, and SW2 near

300 km for the TIEGCM/ICON simulation with constant geophysical forcing (i.e., "Run 2"). The solar/geomagnetic-driven ∼10− to ∼30-day variability in the migrating tides is absent, and the IS variations in DW1 are significantly diminished. Notably, SW2 retains substantial (±16 m/s) low-latitude IS variability, far exceeding those observed in DE2 and DE3 (±5 m/s). This IS variability in SW2 can be attributed to the upward propagating component (ref. Maute et al., 2023), as well as nonlinear interaction processes in the thermosphere, including (a) interactions between SW2 and other tides; (b) interactions with planetary waves or gravity waves; (c) modulation of background fields; and (d) coupling with ionospheric processes. It is beyond the scope of this paper to further investigate these connections; this effort is left for dedicated follow-up studies. Note that the scales in Figures 6–8 are intentionally chosen to vary, as this allows for the effective visualization of the specific variability and amplitude differences within each tidal component and altitude. Consistent scaling across all figures would risk obscuring smaller variations in components with lower amplitudes, thereby reducing the clarity of the presented results. In conclusion, Figures 5–9 collectively underscore the critical importance of tidal forcing in driving IS thermospheric variability. These results indicate that significant IS variability in tidal amplitudes propagates vertically and can considerably impact the thermospheric dynamics. These observations highlight the dynamic and complex nature of tidal forcing in the thermosphere.

As a next step, we aim to further investigate the connection between IS variability in the ZDM thermospheric winds, DE3, and the MJO, as represented by the RMM1 index (ref. Figures 2d1–2d2). To this end, Pearson correlation analyses are performed between the filtered ZDM zonal winds, RMM1, and tidal amplitudes shown in Figures 5–9. All these time series are filtered using the method described in Section 3 to highlight IS variability. Figure 10 presents results from correlation analyses performed on the ZDM zonal winds, the near-equatorial (15°S-15°N mean) DE3 amplitudes, and the RMM1 index. Figure 10a1 (Figure 10b1) shows the time series of DE3 amplitudes (RMM1) and ZDM zonal winds at ∼150 km altitude. The blue lines represent the filtered ZDM zonal winds (Figure 10a1) and RMM1 (Figure 10b1), while the red lines depict the filtered DE3 amplitudes. Figures 10c1–10d1 show the same results as Figures 10a1–10b1 but at ∼300 km altitude.

The left-hand panels of Figure 10 compare ZDM zonal winds with DE3, while the right-hand panels compare RMM1 with DE3. This arrangement highlights distinct aspects of variability: the left panels emphasize the role of atmospheric tides in driving thermospheric variability, while the right panels capture the influence of the MJO on these processes. The lagged correlation plots below each panel (a_2–d_2) provide insights into the timing relationships. A negative lag indicates that the first variable (ZDM zonal wind or RMM1) leads the second variable (DE3), while a positive lag means the reverse. The correlation analysis in Figures 10a2 and 10b2 quantifies the relationships shown in Figures 10a1 and 10b1, respectively. Specifically, Figure 10a2 shows the lagged correlation between DE3 and ZDM zonal winds, while Figure 10b2 shows the correlation between DE3 and RMM1. Using 180-day moving windows, chosen to span twice the maximum ISO period of 90 days, the analysis reveals that DE3 exhibits a notable connection with both ZDM zonal winds and RMM1. For example, Figure 10b2 shows a peak correlation of approximately $r = 0.6$ at a positive lag of around 14 days, indicating that changes in RMM1 precede variations in DE3 amplitudes by about 2 weeks. However, connections between RMM1 and ZDM zonal winds are indirect and mediated through their mutual relationship with DE3. Figures 10c1 and 10d1 extend this analysis to a higher altitude of ∼300 km. The lagged correlations at this altitude (Figures 10c2 and 10d2) display similar patterns to those at ∼150 km, with a peak correlation for DE3 and RMM1 at a positive lag, though with a lower value for the ISO of approximately $r = 0.4$. These results suggest that the MJO's influence on DE3 extends through multiple atmospheric layers into the middle thermosphere, with ZDM zonal winds also responding to DE3 variability. Preliminary analysis of other MJO indices (e.g., RMM2, the OLR-based MJO index (OMI)) suggests that these parameters exhibit slightly different delays in their response (not shown), indicating additional complexities that warrant investigation in dedicated follow-on studies. Figure 10 highlights the significant interaction between the MJO, represented by the RMM1 index, and DE3, as well as the indirect relationship between RMM1 and ZDM zonal winds mediated through DE3. These findings underscore the complex dynamics of atmospheric tides and their modulation by large-scale oscillations like the MJO, which play a crucial role in atmospheric wave coupling and energy transfer processes. To further substantiate the connection between the DE3 tide and the MJO, additional analyses accounting for zonal phase propagation were conducted, providing a clearer demonstration of the relationship between this tidal component and the MJO.

Figure 11a1 presents the Hovmöller diagram of the MJO-filtered near-equatorial (15°S−15°N mean) zonal wind DE3 near 110 km altitude from TIEGCM-ICON. As described in Kumari et al. (2021), the MJO tidal diagnostic adopts a standard Hovmöller analysis (Wheeler & Kiladis, 1999) applied to the tidal anomalies. The steps for

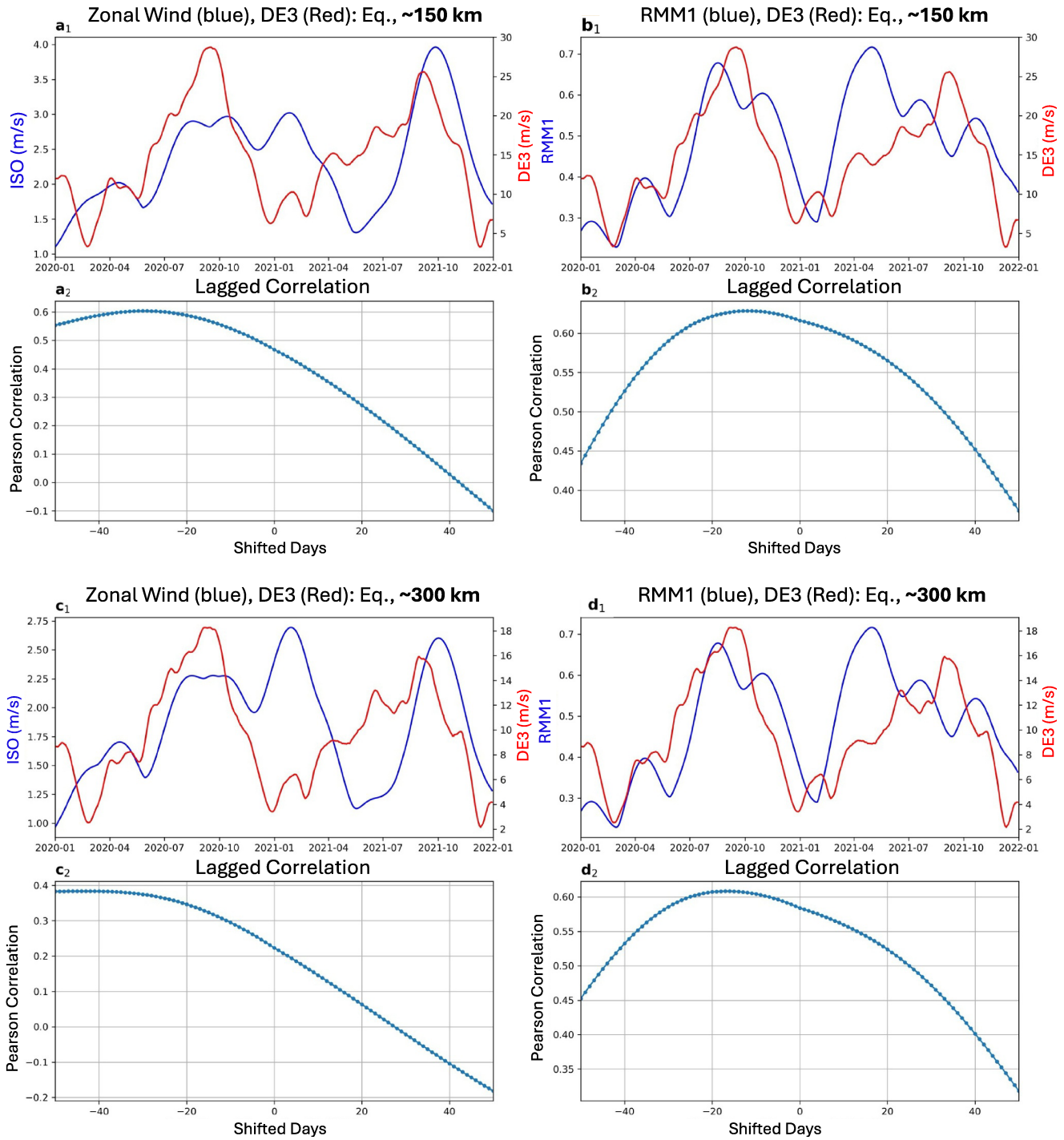

Figure 10. Time series near 150 km (a_1) of 5–90-day filtered near-equatorial (15°S–15°N) zonal and diurnal mean (ZDM) intra-seasonal oscillation (ISO) (blue line, left *y*-axis) and DE3 zonal wind (red line, right *y*-axis) amplitudes and their lagged Pearson correlation coefficient (a_2) was obtained on 180-day moving windows from January 2020 to December 2021. (b_1)–(b_2) Same as panels a_1–a_2, but for RMM1 and near-equatorial DE3 zonal wind amplitudes. (c_1)–(c_2) and (d_1)–(d_2) Same as (a_1)–(a_2), and (b_1)–(b_2), respectively, but near 300 km altitude. The DE3 zonal winds and ZDM ISOs are derived from TIEGCM-ICON "Run 1" output.

Hovmöller analysis are as follows: (a) tidal perturbations are computed for each day as a function of latitude and longitude, (b) daily climatology is computed by averaging the perturbations over multiple years (e.g., 2 or more), (c) deviations (anomalies) from the climatology for each day are computed, (d) a 30–90 days bandpass filter is

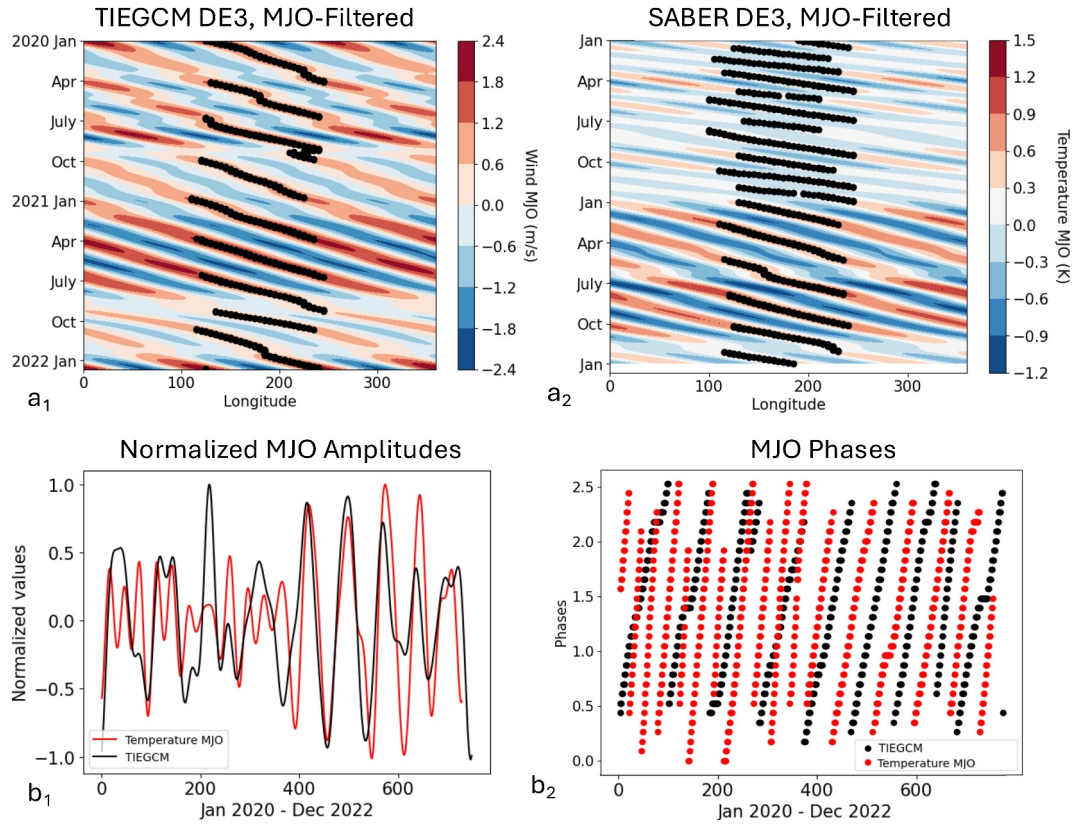

Figure 11. Hovmöller Madden-Julian Oscillation (MJO) analyses of DE3 during 2020–2021 near 110 km altitude and the equator (15°S–15°N mean) for TIEGCM-ICON zonal wind (a_1) and SABER temperature (panel a_2). The SABER DE3 amplitude and phases are obtained from 45-day moving windows using the tidal deconvolution method by Oberheide et al. (2002). The overplotted back dots in (a_1) and (a_2) show the MJO phases, that is, the location of maximum amplitude between longitude range 100°–250°. (b_1) Normalized DE3 amplitudes based on the MJO filtered series in panels (a_1)–(a_2), with SABER temperature DE3 shown as a red line and Thermosphere Ionosphere Electrodynamics General Circulation Model zonal wind DE3 shown as a black line. (b_2) Same depiction as (b_1), but showing the respective MJO phases (i.e., the location of max amplitude, in radians).

applied, and (e) the eastward-propagating signal is extracted. Figure 11a2 displays the SABER temperature DE3 similarly filtered for the MJO component. The color bar indicates wind (temperature) deviations in m/s (K), with positive anomalies shown in red and negative anomalies in blue. The *y*-axis displays the time progression from January 2020 to January 2022, while the *x*-axis represents longitude. Note that the SABER DE3 tidal amplitudes and phases are obtained using 45-day moving windows, applying the tidal deconvolution method described by Oberheide et al. (2002). This method allows for the isolation and analysis of specific tidal components by filtering out other tidal and non-tidal variations. Both Figures 11a1 and 11a2 reveal the longitudinal propagation of the MJO signal, characterized by eastward propagation and alternating patterns of positive and negative anomalies every ∼30–90 days. The location of the maximum amplitude within the longitude range of ∼100° −250° is indicated by an overplotted black line, illustrating the overall coherence of the eastward-propagating phase progression.

Figure 11b1 illustrates the normalized amplitudes of the DE3 tidal component, derived from the MJO-filtered series in Figures 11a1 and 11a2. The SABER MJO-filtered temperature DE3 amplitudes are depicted as a red line, while the TIEGCM MJO-filtered zonal wind DE3 amplitudes are shown as a black line. The *x*-axis covers the period from January 2020 to December 2022, and the *y*-axis represents normalized values ranging from −1 to 1. The synchronization between the red and black lines indicates clear connections between the temperature and wind DE3 responses to the MJO near 110 km altitude, demonstrating the coherent behavior of the MJO signal in the DE3 component in both temperature and wind fields. To explore this connection further, we have also examined the phase progression of the DE3 component (Figure 11b2). Even during periods where the amplitudes

differ, the phase consistency between TIEGCM-ICON and SABER suggests that while the strength of the signal varies, the underlying dynamical processes remain similar. Note some observed discrepancy in amplitude between TIEGCM and SABER, particularly during June-December 2020. Several factors could contribute to this mismatch: (a) SABER, which measures temperature, might not capture variations as effectively at certain altitudes or regions where TIEGCM-ICON shows stronger wind-driven variability. Differences in data coverage between SABER and ICON could also lead to these discrepancies, especially in lower amplitude periods. (b) The SABER data are processed using 45-day moving windows, which may smooth out some of the finer variability seen in the TIEGCM-ICON output, particularly in periods where the signal amplitude is lower. TIEGCM, on the other hand, could retain higher resolution or variability due to its model assumptions. (c) The temperature response observed by SABER may be influenced by different processes than the zonal wind response in TIEGCM-ICON. The lack of a strong temperature response in parts of 2020 could indicate that while the dynamical forcing was strong, the thermodynamic coupling to the temperature field was weaker, leading to a reduced amplitude in SABER. (d) While the amplitudes may not match perfectly during lower-amplitude periods, the phase progression of the DE3 component is generally consistent, as demonstrated by Figure 11b2. As discussed by Kumari et al. (2021), a statistical analysis with a longer data set may be needed for a more robust amplitude and phase comparison, which is out of scope for this study. Despite these model/data differences, Figure 11 provides a comprehensive view of the MJO's influence on the DE3 tidal component, showcasing the longitudinal propagation of temperature and wind anomalies. The normalized amplitudes in Figure 11b1 and phases in Figure 11b2 highlight a general consistent response of these anomalies to the MJO, demonstrating a clear connection between DE3 and the MJO and agreement between the MJO signal in SABER and TIEGCM DE3 amplitudes.

5. Conclusions

In this study, an ICON-adapted version of the TIEGCM, incorporating LB tides derived from MIGHTI observations, was used to characterize and quantify the impact of the upward-propagating tidal spectrum on thermospheric intra-seasonal (IS) oscillations (ISOs) and to elucidate connections to the MJO. Results show that thermospheric ZDM zonal winds exhibit prominent (∼20 m/s) tidally driven ISOs throughout 2020–2021, with the largest variations occurring at low latitudes (±30°) near ∼110–150 km altitude. Correlation analyses demonstrate a robust (r>0.6) connection between the thermospheric ISOs, tides, and the tropospheric MJO, while Hovmöller diagrams indicate eastward tidal propagation consistent with the MJO and concurrent SABER observations.

Key findings include:

1. Tidal Contributions to Thermospheric ISOs: Results show that the diurnal/semidiurnal tidal spectrum entering the lower thermosphere near 97 km is a leading source of IS variability in the ZDM zonal wind over the whole (∼100–400 km) thermosphere. Notably, a large ∼64-day periodicity in ZDM zonal winds aligns with similar periodicities observed in OLR and RMM1 and is demonstrated to be both tidal- and MJO-related.
2. Altitude and Latitude Dependence: Altitude-time contours of ZDM zonal winds reveal that the most substantial IS variations occur in the lower thermosphere, particularly around 110–130 km. However, these variations also extend well into the middle and upper thermosphere, indicating that tidal influences penetrate multiple atmospheric layers. The latitude-time structures further highlight the complex interplay between tidal components and background wind fields, with distinct equatorially symmetric and asymmetric patterns emerging throughout the year.
3. Influence of Tidal Forcing: Comparative analysis of different TIEGCM-ICON simulations underscores the importance of tidal forcing in driving IS variability. Runs with realistic tidal forcing at the LB exhibit pronounced IS variations, while simulations with constant geophysical forcing predominantly show solar/geomagnetic-induced periodicities without significant IS variations. This result highlights the critical role of tidal inputs in shaping thermospheric dynamics around IS timescales.
4. MJO-Thermosphere Interaction: Correlation analyses reveal a significant interaction between the MJO, represented by the RMM1 index, and thermospheric DE3 amplitudes. A peak correlation of approximately $r = 0.6$ at a positive lag of around 14 days indicates that MJO variations precede changes in DE3 amplitudes by about 2 weeks, suggesting a coherent vertical coupling mechanism within the atmospheric column. Comparisons between DE3 and ZDM zonal winds show similarly strong correlations, with lags indicating that DE3 variability is closely tied to the dynamical tides. No direct correlations between RMM1 and ZDM winds

are presented; their connection is inferred indirectly through their shared relationship with DE3. This interaction is observed across multiple altitudes, with peak correlations at ~150 km and ~ 300 km showing consistent patterns, albeit with slightly reduced magnitudes at higher altitudes. These findings demonstrate the far-reaching influence of the MJO on thermospheric dynamics and the critical role of atmospheric tides in mediating this connection.

5. Hovmöller Diagram Analyses: Hovmöller diagnostics of MJO-filtered DE3 components from TIEGCM-ICON and SABER data reveal eastward propagation patterns consistent with the MJO, further corroborating the link between MJO activity and thermospheric tidal responses. The synchronization of DE3 amplitudes between TIEGCM-ICON winds and SABER temperatures underscores the coherent behavior of the MJO influence in the thermosphere.

This study underscores the intricate dynamics of atmospheric tides and their modulation by large-scale tropospheric oscillations, such as the MJO. These interactions have profound implications for the global understanding of wave coupling and energy transfer processes. Our findings reveal the complex interplay between lower atmospheric processes and thermospheric dynamics on IS time scales, highlighting the necessity for comprehensive modeling and observational frameworks to enhance our understanding of vertical coupling mechanisms. Improving our understanding of the thermosphere has widespread practical applications that benefit satellite operations, communication systems, weather and climate prediction, defense and security, scientific research, and aviation.

Future research should focus on further quantifying these interactions and exploring their implications for thermosphere-ionosphere (T-I) states and dynamics. These efforts are expected to provide valuable insights for the development of predictive capabilities that connect tropical tropospheric weather to space weather of the T-I system. This study also emphasizes the critical need for detailed investigations into the vertical and horizontal coupling mechanisms within the "thermospheric gap" region, spanning approximately 100–300 km. Such investigations will be uniquely enabled by a new dedicated satellite mission designed to provide simultaneous global measurements of this region.

Data Availability Statement

TIEGCM-ICON output is available from Coordinated Data Analysis Web (2024), the Kp index is obtained from Kp.gfz-potsdam (2024), the F10.7 cm radio flux from OMNIWeb (2024). NOAA Interpolated Outgoing Longwave Radiation (OLR) data and Real-time Multivariate MJO series 1 (RMM1) index values are provided by PSL.noaa.gov (2024). The post-processed data used to produce Figures 1–11 are publicly available at Gasperini (2024).

Acknowledgments
FG acknowledges support from NSF Grants 2113411 and 2223930; NASA Grants 80NSSC22K0019 and 80NSSC22K1010; and AFOSR Grant FA9550-22-1-0328. ICON is supported by NASA's Explorers Program through contracts NNG12FA45C and NNG12FA42I. AM acknowledges support from NASA ICON award 80NSSC23K1123 and NASA LWS award 80NSSC20K1784.

References

Alken, P., Thébault, E., Beggan, C. D., Amit, H., Aubert, J., Baerenzung, J., et al. (2021). International Geomagnetic Reference Field: The thirteenth generation. *Earth Planets and Space*, *73*(1), 49. https://doi.org/10.1186/s40623-020-01288-x

Andrews, D. G., Holton, J. R., & Leovy, C. B. (1987). *Middle atmospheric dynamics* (p. 489). Academic Press.

CDAWeb. (2024). Coordinated Data Analysis Web (CDAWEB) [Dataset]. *GSFC/SPDF*. Retrieved from https://cdaweb.gsfc.nasa.gov/pub/data/icon

Chang, L. C., Palo, S. E., & Liu, H. (2011). Short-term variability in the migrating diurnal tide caused by interactions with the quasi 2 day wave. *Journal of Geophysical Research*, *116*(D12), D12112. https://doi.org/10.1029/2010JD014996

Chapman, S., & Lindzen, R. S. (1970). *Atmospheric tides*. Reidel.

Cullens, C. Y., England, S. L., Immel, T. J., Maute, A., Harding, B. J., Triplett, C. C., et al. (2022). Seasonal variations of medium-scale waves observed by icon-mighty. *Geophysical Research Letters*, *49*(17), e2022GL099383. https://doi.org/10.1029/2022gl099383

Cullens, C. Y., Immel, T. J., Triplett, C. C., Wu, Y. J., England, S. L., Forbes, J. M., & Liu, G. (2020). Sensitivity study for ICON tidal analysis. *Progress in Earth and Planetary Science*, *7*(1), 18. https://doi.org/10.1186/s40645-020-00330-6

Dickinson, R. E. (1984). Infrared radiative cooling in the mesosphere and lower thermosphere. *Journal of Atmospheric and Terrestrial Physics*, *46*(11), 995–1008. https://doi.org/10.1016/0021-9169(84)90006-0

Drob, D. P., Emmert, J. T., Meriwether, J. W., Makela, J. J., Doornbos, E., Conde, M., et al. (2015). An update to the horizontal wind model (HWM): The quiet time thermosphere. *Earth and Space Science*, *2*(7), 301–319. https://doi.org/10.1002/2014EA000089

Eckermann, S. D., Rajopadhyaya, D. K., & Vincent, R. A. (1997). Intraseasonal wind variability in the equatorial mesosphere and lower thermosphere: Long-term observations from the central Pacific. *Journal of Atmospheric and Solar-Terrestrial Physics*, *59*(6), 603–627. https://doi.org/10.1016/S1364-6826(96)00143-5

Forbes, J. M. (1995). Tidal and planetary waves. *Geophysics Monographs*, *87*, 67–87. https://doi.org/10.1029/gm087p0067

Forbes, J. M. (2000). Wave coupling between the lower and upper atmosphere: Case study of an ultra-fast Kelvin wave. *Journal of Atmospheric and Solar-Terrestrial Physics*, *62*(17–18), 1603–1621. https://doi.org/10.1016/s1364-6826(00)00115-2

Forbes, J. M., Bruinsma, S., & Lemoine, F. G. (2006). Solar rotation effects on the thermospheres of Mars and Earth. *Science*, *312*(5778), 1366–1368. https://doi.org/10.1126/science.1126389

Forbes, J. M., & Hagan, M. E. (1982). Thermospheric extensions of the classical expansion functions for semidiurnal tides. *Journal of Geophysical Research*, *87*(A7), 5253–5259. https://doi.org/10.1029/JA087iA07p05253

Forbes, J. M., Heelis, R., Zhang, X., Englert, C. R., Harding, B. J., He, M., et al. (2021). Q2DW-tide and-ionosphere interactions as observed from ICON and ground-based radars. *Journal of Geophysical Research: Space Physics*, *126*(11). https://doi.org/10.1029/2021JA029961

Forbes, J. M., Oberheide, J., Zhang, X., Cullens, C., Englert, C. R., Harding, B. J., et al. (2022). Vertical coupling by solar semidiurnal tides in the thermosphere from ICON/MIGHTI measurements. *Journal of Geophysical Research: Space Physics*, *127*(5), e2022JA030288. https://doi.org/10.1029/2022JA030288

Forbes, J. M., & Vincent, R. A. (1989). Effects of mean winds and dissipation on the diurnal propagating tide: An analytic approach. *Planetary and Space Science*, *37*(2), 197–209. https://doi.org/10.1016/0032-0633(89)90007-x

Forbes, J. M., & Zhang, X. (2022). Hough Mode Extensions (HMEs) and solar tide behavior in the dissipative thermosphere. *Journal of Geophysical Research: Space Physics*, *127*(11), e2022JA030962. https://doi.org/10.1029/2022JA030962

Forbes, J. M., Zhang, X., Englert, C. R., Heelis, R., Stevens, M. H., Harding, B. J., et al. (2024). Thermosphere UFKW structures and ionosphere coupling as observed by ICON. *Geophysical Research Letters*, *51*(8), e2023GL105975. https://doi.org/10.1029/2023GL105975

Forbes, J. M., Zhang, X., Hagan, M. E., England, S. L., Liu, G., & Gasperini, F. (2017). On the specification of upward-propagating tides for ICON science investigations. *Space Science Reviews*, *212*(1–2), 697–713. https://doi.org/10.1007/s11214-017-0401-5

Forbes, J. M., Zhang, X., Heelis, R., Stoneback, R., Englert, C. R., Harlander, J. M., et al. (2021). Atmosphere-ionosphere (A-I) coupling as viewed by ICON: Day-to-day variability due to planetary wave (PW)-tide interactions. *Journal of Geophysical Research: Space Physics*, *126*(6), e2020JA028927. https://doi.org/10.1029/2020JA028927

Forbes, J. M., Zhang, X., & Palo, S. E. (2023). UFKW propagation in the dissipative thermosphere. *Journal of Geophysical Research: Space Physics*, *128*(1), e2022JA030921. https://doi.org/10.1029/2022JA030921

Forbes, J. M., Zhang, X., Palo, S. E., Russell, J., Mertens, C. J., & Mlynczak, M. (2009). Kelvin waves in stratosphere, mesosphere and lower thermosphere temperatures as observed by TIMED/SABER during 2002-2006. *Earth Planets and Space*, *61*(4), 447–453. https://doi.org/10.1186/bf03353161

Forbes, J. M., Zhang, X., Talaat, E. R., & Ward, W. (2003). Nonmigrating diurnal tides in the thermosphere. *Journal of Geophysical Research*, *108*(A1), 1033. https://doi.org/10.1029/2002JA009262

Fritts, D. C., & Alexander, M. J. (2003). Gravity wave dynamics and effects in the middle atmosphere. *Reviews of Geophysics*, *41*(1), 1003. https://doi.org/10.1029/2001rg000106

Gasperini. (2024). Zenodo data and software files [Dataset]. https://zenodo.org/records/12744701

Gasperini, F., Azeem, I., Crowley, G., Perdue, M., Depew, M., Immel, T., et al. (2021). Dynamical coupling between the low-latitude lower thermosphere and ionosphere via the nonmigrating diurnal tide as revealed by concurrent satellite observations and numerical modeling. *Geophysical Research Letters*, *48*(14), e2021GL093277. https://doi.org/10.1029/2021GL093277

Gasperini, F., Crowley, G., Immel, T. J., & Harding, B. J. (2022). Vertical wave coupling in the low-latitude ionosphere-thermosphere as revealed by concurrent ICON and COSMIC-2 observations. *Space Science Reviews*, *218*(7), 55. https://doi.org/10.1007/s11214-022-00923-1

Gasperini, F., Forbes, J. M., Doornbos, E. N., & Bruinsma, S. L. (2015). Wave coupling between the lower and middle thermosphere as viewed from TIMED and GOCE. *Journal of Geophysical Research*, *120*(7), 5788–5804. https://doi.org/10.1002/2015JA021300

Gasperini, F., Forbes, J. M., Doornbos, E. N., & Bruinsma, S. L. (2018). Kelvin wave coupling from TIMED and GOCE: Inter/intra-annual variability and solar activity effects. *Journal of Atmospheric and Solar-Terrestrial Physics*, *171*, 176–187. https://doi.org/10.1016/j.jastp.2017.08.034

Gasperini, F., Forbes, J. M., & Hagan, M. E. (2017a). Wave coupling from the lower to the middle thermosphere: Effects of mean winds and dissipation. *Journal of Geophysical Research*, *122*(7), 7781–7797. https://doi.org/10.1002/2017JA024317

Gasperini, F., Hagan, M. E., & Zhao, Y. (2017b). Evidence of tropospheric 90-day oscillations in the thermosphere. *Geophysical Research Letters*, *44*(20). https://doi.org/10.1002/2017GL075445

Gasperini, F., Harding, B. J., Crowley, G., & Immel, T. J. (2023a). Ionosphere-thermosphere coupling via global-scale waves: New insights from two years of concurrent in situ and remotely-sensed satellite observations. *Frontiers in Astronomy and Space Sciences*, *10*, 1217737. https://doi.org/10.3389/fspas.2023.1217737

Gasperini, F., Jones, M., Jr., Harding, B. J., & Immel, T. J. (2023b). Direct observational evidence of altered mesosphere lower thermosphere mean circulation from a major sudden stratospheric warming. *Geophysical Research Letters*, *50*(7), e2022GL102579. https://doi.org/10.1029/2022GL102579

Gasperini, F., Jr., Moffat-Griffin, T., Marsh, D., Cullens, C., & Knizova, P. K. (2023c). Ionosphere-thermosphere-mesosphere variability imposed by waves from below in future climates. *Bulletin of the AAS*, *55*(3). https://doi.org/10.3847/25c2cfeb.c3db219f

Gasperini, F., Liu, H., & McInerney, J. (2020). Preliminary evidence of Madden-Julian Oscillation effects on ultrafast tropical waves in the thermosphere. *Journal of Geophysical Research*, *125*(5), e2019JA027649. https://doi.org/10.1029/2019JA027649

Gasperini, F., & Oberheide, J. (2024). Dynamical meteorology: Atmospheric tides. *Reference Module in Earth Systems and Environmental Sciences*. https://doi.org/10.1016/B978-0-323-96026-7.00073-4

Gruber, A., & Winston, J. S. (1978). Earth-atmosphere radiative heating based on NOAA scanning radiometer measurements. *Bulletin of the American Meteorological Society*, *59*(12), 1570–1573. https://doi.org/10.1175/1520-0477(1978)059<1570:earhbo>2.0.co;2

Gu, S.-Y., Dou, X., Lei, J., Li, T., Luan, X., Wan, W., & Russell, J. M. III. (2014). Ionospheric response to the ultrafast Kelvin wave in the MLT region. *Journal of Geophysical Research*, *119*(2), 1369–1380. https://doi.org/10.1002/2013JA019086

Hagan, M. E., & Forbes, J. M. (2002). Migrating and nonmigrating diurnal tides in the middle and upper atmosphere excited by tropospheric latent heat release. *Journal of Geophysical Research*, *107*(D24), 4754. https://doi.org/10.1029/2001JD001236

Hagan, M., Forbes, J., & Vial, F. (1995). On modeling migrating solar tides. *Geophysical Research Letters*, *22*(8), 893–896. https://doi.org/10.1029/95GL00783

Hagan, M. E., Maute, A., Roble, R. G., Richmond, A. D., Immel, T. J., & England, S. L. (2007). Connections between deep tropical clouds and the Earth's ionosphere. *Geophysical Research Letters*, *34*, L20109. https://doi.org/10.1029/2007GL030142

Harding, B. J., Chau, J. L., He, M., Englert, C. R., Harlander, J. M., Marr, K. D., et al. (2021). Validation of ICON-MIGHTI thermospheric wind observations: 2. Green-line comparisons to specular meteor radars. *Journal of Geophysical Research: Space Physics*, *126*(3), 1–12. https://doi.org/10.1029/2020JA028947

Harding, B. J., Immel, T. J., Mende, S. B., Wu, Y.-J. J., Maute, A., England, S. L., et al. (2024). Day-to-day variability of the neutral wind dynamo observed by ICON: First results from conjugate observations. *Geophysical Research Letters*, *51*(5), e2023GL107110. https://doi.org/10.1029/2023GL107110

Hayashi, Y. (1971). A generalized method of resolving disturbances into progressive and retrogressive waves by space Fourier and time cross-spectral analyses. *Journal of the Meteorological Society of Japan. Series II*, *49*(2), 125–128. https://doi.org/10.2151/jmsj1965.49.2_125

Hughes, J., Gasperini, F., & Forbes, J. M. (2022). Solar rotation effects in Martian thermospheric density as revealed by five years of MAVEN observations. *Journal of Geophysical Research: Planets*, *127*, e2021JE007036. https://doi.org/10.1029/2021JE007036

Immel, T. J., & Eastes, R. W. (2019). New NASA missions focus on terrestrial forcing of the space environment. *Bulletin of the American Meteorological Society*, *100*(11), 2153–2156. https://doi.org/10.1175/BAMS-D-19-0066.1

Immel, T. J., England, S. L., Mende, S. B., Heelis, R. A., Englert, C. R., Edelstein, J., et al. (2018). The ionospheric connection explorer mission: Mission goals and design. *Space Science Reviews*, *214*(1), 13. https://doi.org/10.1007/s11214-017-0449-2

Immel, T. J., Harding, B. J., Heelis, R. A., Maute, A., Forbes, J. M., England, S. L., et al. (2021). Regulation of ionospheric plasma velocities by thermospheric winds. *Nature Geoscience*, *14*(12), 893–898. https://doi.org/10.1038/s41561-021-00848-4

Johnson, E. S., & Heelis, R. A. (2005). Characteristics of ion velocity structure at high latitudes during steady southward interplanetary magnetic field conditions. *Journal of Geophysical Research*, *110*(A12), 148–227. https://doi.org/10.1029/2005ja011130

Jones, M., Forbes, J. M., Hagan, M. E., & Maute, A. (2014). Impacts of vertically propagating tides on the mean state of the ionosphere-thermosphere system. *Journal of Geophysical Research: Space Physics*, *119*(3), 2197–2213. https://doi.org/10.1002/2013ja019744

Karoly, D. J., Roff, G. L., & Reeder, M. J. (1996). Gravity wave activity associated with tropical convection detected in TOGA COARE sounding data. *Geophysical Research Letters*, *23*(3), 261–264. https://doi.org/10.1029/96GL00023

Kayano, M. T., Kousky, V. E., & Janowiak, J. E. (1995). Outgoing longwave radiation bias and their impacts on EOF modes of interannual variability in the Tropics. *Journal of Geophysical Research*, *100*, 3173–3195.

Kp.gfz-potsdam. (2024). Geomagnetic Kp index [Dataset]. https://kp.gfz-potsdam.de/app/files/Kp_ap_since_1932.txt

Kumari, K., Oberheide, J., & Lu, X. (2020). The tidal response in the mesosphere/lower thermosphere to the Madden-Julian oscillation observed by SABER. *Geophysical Research Letters*, *47*(16), e2020GL089172. https://doi.org/10.1029/2020GL089172

Kumari, K., Wu, H., Long, A., Lu, X., & Oberheide, J. (2021). Mechanism studies of Madden-Julian Oscillation coupling into the mesosphere/lower thermosphere tides using SABER, MERRA-2, and SD-WACCMX. *Journal of Geophysical Research: Atmospheres*, *126*(13), e2021JD034595. https://doi.org/10.1029/2021JD034595

Li, J., & Lu, X. (2021). Global responses of gravity waves and zonal mean winds to the Madden-Julian oscillation and the latitudinal dependence of their relations using MERRA-2. *Geophysical Research Letters*, *48*(20), e2021GL094717. https://doi.org/10.1029/2021GL094717

Li, J., & Lu, X. (2020). SABER observations of gravity wave responses to the Madden-Julian oscillation from the stratosphere to the lower thermosphere in tropics and extratropics. *Geophysical Research Letters*, *47*(23), e2020GL091014. https://doi.org/10.1029/2020GL091014

Li, X., Ren, Z., & Cao, J. (2024). The non-migrating DE3 tide response to the MJO phenomenon at the MLT altitudes. *Journal of Geophysical Research: Space Physics*, *129*(10), e2024JA032792. https://doi.org/10.1029/2024JA032792

Lieberman, R. S. (1998). Intraseasonal variability of high-resolution Doppler imager winds in the equatorial mesosphere and lower thermosphere. *Journal of Geophysical Research*, *103*(D10), 11221–11228. https://doi.org/10.1029/98jd00532

Lieberman, R. S., Riggin, D. M., Ortland, D. A., Nesbitt, S. W., & Vincent, R. A. (2007). Variability of mesospheric diurnal tides and tropospheric diurnal heating during 1997-1998. *Journal of Geophysical Research*, *112*(D20), D20110. https://doi.org/10.1029/2007JD008578

Liebmann, B., & Smith, C. A. (1996). Description of a complete (interpolated) Outgoing Longwave Radiation dataset. *Bulletin of the American Meteorological Society*, *77*, 1275–1277.

Lindzen, R. S., & Hong, S. S. (1974). Effects of mean winds and horizontal temperature gradients on solar and lunar semidiurnal tides in the atmosphere. *Journal of the Atmospheric Sciences*, *31*(5), 1421–1446. https://doi.org/10.1175/1520-0469(1974)031<1421:eomwah>2.0.co;2

Liu, H.-L. (2016). Variability and predictability of the space environment as related to lower atmosphere forcing. *Space Weather*, *14*(9), 634–658. https://doi.org/10.1002/2016SW001450

Liu, Y., San Liang, X., & Weisberg, R. H. (2007). Rectification of the bias in the wavelet power spectrum. *Journal of Atmospheric and Oceanic Technology*, *24*(12), 2093–2102. https://doi.org/10.1175/2007JTECHO511.1

Madden, R. A., & Julian, P. R. (1971). Detection of a 40-50 day oscillation in the zonal wind in the tropical Pacific. *Journal of Geophysical Research*, *28*(5), 702–708. https://doi.org/10.1175/1520-0469(1971)028<0702:doadoi>2.0.co;2

Madden, R. A., & Julian, P. R. (1994). Observations of the 40-50-day tropical oscillation: A review. *Monthly Weather Review*, *122*(5), 814–837. https://doi.org/10.1175/1520-0493(1994)122<0814:OOTDTO>2.0.CO;2

Matsushita, S. (1967a). Solar quiet and lunar daily variation fields. In S. Matsushita & W. H. Campbell (Eds.), *Physics of geomagnetic phenomena* (pp. 301–427). Academic Press.

Matsushita, S. (1967b). Lunar tides in the ionosphere. In *Handbuch der Physik* (pp. 547–602). Springer-Verlag.

Maute, A. (2017). Thermosphere-ionosphere-electrodynamics general circulation model for the ionospheric connection explorer: TIEGCM-ICON. *Space Science Reviews*, *212*(1–2), 523–551. https://doi.org/10.1007/s11214-017-0330-3

Maute, A., Forbes, J. M., Cullens, C. Y., & Immel, T. J. (2023). Delineating the effect of upward propagating migrating solar tides with the TIEGCM-ICON. *Frontiers in Astronomy and Space Sciences*, *10*, 1147571. https://doi.org/10.3389/fspas.2023.1147571

Mertens, C. J., Mlynczak, M. G., Lopez-Puertas, M., Wintersteiner, P. P., Picard, R. H., Winick, J. R., et al. (2003). Retrieval of kinetic temperature and carbon dioxide abundance from non-local thermodynamic equilibrium limb emission measurements made by the SABER experiment on the TIMED satellite. *The International Society for Optical Engineering*, *4882*, 162–171. https://doi.org/10.1117/12.463358

Moss, A. C., Wright, C. J., & Mitchell, N. J. (2016). Does the Madden-Julian oscillation modulate stratospheric gravity waves? *Geophysical Research Letters*, *43*(8), 3973–3981. https://doi.org/10.1002/2016GL068498

Oberheide, J., Forbes, J. M., Zhang, X., & Bruinsma, S. L. (2011a). Climatology of upward propagating diurnal and semidiurnal tides in the thermosphere. *Journal of Geophysical Research*, *116*(A11). https://doi.org/10.1029/2011JA01678

Oberheide, J., Forbes, J. M., Zhang, X., & Bruinsma, S. L. (2011b). Wave-driven variability in the ionosphere-thermosphere-mesosphere system from TIMED observations: What contributes to the "wave 4"? *Journal of Geophysical Research*, *116*(A1). https://doi.org/10.1029/2010JA015911

Oberheide, J., Hagan, M. E., Roble, R. G., & Offermann, D. (2002). Sources of nonmigrating tides in the tropical middle atmosphere. *Journal of Geophysical Research*, *107*(D21), 4567. https://doi.org/10.1029/2002JD002220

OMNIWeb. (2024). Solar flux data [Dataset]. https://www.spaceweather.gc.ca/solar_flux_data/daily_flux_values/fluxtable.txt

Palo, S. E., Roble, R. G., & Hagan, M. E. (1999). Middle atmosphere effects of the quasi-two-day wave determined from a General Circulation Model. *Earth Planets and Space*, *51*(7–8), 629–647. https://doi.org/10.1186/bf03353221

Pancheva, D., Miyoshi, Y., Mukhtarov, P., Jin, H., Shinagawa, H. H., & Fujiwara, H. (2012). Global response of the ionosphere to atmospheric tides forced from below: Comparison between cosmic measurements and simulations by atmosphere-ionosphere coupled model GAIA. *Journal of Geophysical Research*, *117*(A7). https://doi.org/10.1029/2011ja017452

Picone, J. M., Hedin, A. E., Drob, D. P., & Aikin, A. C. (2002). Nrlmsise-00 empirical model of the atmosphere: Statistical comparisons and scientific issues. *Journal of Geophysical Research*, *107*(A12). https://doi.org/10.1029/2002JA009430

PSL.noaa.gov. (2024). Outgoing longwave radiation (OLR) data and RMM index [Dataset]. https://psl.noaa.gov/data/gridded/data.olrcdr.interp.html

Qian, L., Burns, A. G., Emery, B. A., Foster, B., Lu, G., Maute, A., et al. (2014). The NCAR TIE-GCM. In J. Huba, R. Schunk, & G. Khazanov (Eds.), *Modeling the ionosphere–thermosphere system*. https://doi.org/10.1002/9781118704417.ch7

Qian, L., & Solomon, S. C. (2012). Thermospheric density: An overview of temporal and spatial variations. *Space Science Reviews*, *168*(1–4), 147–173. https://doi.org/10.1007/s11214-011-9810-z

Remsberg, E. E., Marshall, B. T., Garcia-Comas, M., Krueger, D., Lingenfelser, G. S., Martin-Torres, J., et al. (2008). Assessment of the quality of the Version 1.07 temperature-versus-pressure profiles of the middle atmosphere from TIMED/SABER. *Journal of Geophysical Research*, *113*, D17101. https://doi.org/10.1029/2008JD010013

Richards, P., Fennelly, J., & Torr, D. (1994). EUVAC: A solar EUV flux model for aeronomic calculations. *Journal of Geophysical Research*, *99*(A5), 8981–8992. https://doi.org/10.1029/94ja00518

Richmond, A. (1995). Ionospheric electrodynamics using magnetic apex coordinates. *Journal of Geomagnetism and Geoelectricity*, *47*(2), 191–212. https://doi.org/10.5636/jgg.47.191

Richmond, A. D., & Maute, A. (2013). Ionospheric electrodynamics modeling. In R. S. J. D. Huba & G. Khazanov (Eds.), *Geophysical monograph series, modeling the ionosphere-thermosphere. AGU geophysical monograph series* (Vol. 201, p. 417). Wiley. https://doi.org/10.1002/9781118704

Richmond, A. D., Ridley, E. C., & Roble, R. G. (1992). A thermosphere/ionosphere general circulation model with coupled electrodynamics. *Geophysical Research Letters*, *19*(6), 601–604. https://doi.org/10.1029/92GL00401

Roble, R., & Ridley, E. (1987). An auroral model for the NCAR thermospheric general circulation model (TGCM). *Annales Geophysicae*, *5A*, 369–382.

Roble, R., Ridley, E., Richmond, A., & Dickinson, R. E. (1988). A coupled thermosphere/ionosphere general circulation model. *Geophysical Research Letters*, *15*(12), 1325–1328. https://doi.org/10.1029/gl015i012p01325

Russell, J. M., III, Mlynczak, M. G., Gordley, L. L., Tansock, J., & Esplin, R. (1999). An overview of the SABER experiment and preliminary calibration results. *The International Society for Optical Engineering*, *3756*, 277–288.

Salby, M. L., Hartmann, D. L., Bailey, P. L., & Gille, J. C. (1984). Evidence for equatorial Kelvin modes in Nimbus-7 LIMS. *Journal of the Atmospheric Sciences*, *41*(2), 220–235. https://doi.org/10.1175/1520-0469(1984)041<0220:efekmi>2.0.co;2

Sassi, F., McCormack, J. P., & McDonald, S. E. (2019). Whole atmosphere coupling on intraseasonal and interseasonal time scales: A potential source of increased predictive capability. *Radio Science*, *54*(11), 913–933. https://doi.org/10.1029/2019RS006847

Stevens, M. H., Englert, C. R., Harlander, J. M., Marr, K. D., Harding, B. J., Triplett, C. C., et al. (2022). Temperatures in the upper mesosphere and lower thermosphere from O2 atmospheric band emission observed by ICON/MIGHTI. *Space Science Reviews*, *218*(8), 67. https://doi.org/10.1007/s11214-022-00935-x

Sutton, J. P. T., Wang, W., Solomon, S. C., Liu, X., & Foster, B. T. (2015). A self-consistent model of helium in the thermosphere. *Journal of Geophysical Research: Space Physics*, *120*(8), 6884–6900. https://doi.org/10.1002/2015JA021223

Talaat, E. R., & Lieberman, R. S. (1999). Nonmigrating diurnal tides in mesospheric and lower thermospheric winds and temperatures. *Journal of the Atmospheric Sciences*, *56*, 4073–4087.

Thayer, J. P., & Semeter, J. (2004). The convergence of magnetospheric energy flux in the polar atmosphere. *Journal of Atmospheric and Solar-Terrestrial Physics*, *66*(10), 807–824. https://doi.org/10.1016/j.jastp.2004.01.035

Tian, B., Ao, C. O., Waliser, D. E., Fetzer, E. J., Mannucci, A. J., & Teixeira, J. (2012). Intraseasonal temperature variability in the upper troposphere and lower stratosphere from GPS radio occultation measurements. *Journal of Geophysical Research*, *117*(D15), D15110. https://doi.org/10.1029/2012JD017715

Torrence, C., & Compo, G. P. (1998). A practical guide to wavelet analysis. *Bulletin of the American Meteorological Society*, *79*(1), 61–78. https://doi.org/10.1175/1520-0477(1998)079<0061:APGTWA>2.0.CO;2

Truskowski, A., Forbes, J. M., Zhang, X., & Palo, S. (2014). New perspectives on thermosphere tides: 1. Lower thermosphere spectra and seasonal-latitudinal structures. *Earth Planets and Space*, *66*, 136. https://doi.org/10.1186/s40623-014-0136-4

Vergados, P., Liu, G., Mannucci, A. J., & Janches, D. (2018). Equatorial intraseasonal temperature oscillations in the lower thermosphere from SABER. *Geophysical Research Letters*, *45*(20), 10893–10902. https://doi.org/10.1029/2018GL079467

Walterscheid, R. L., & Venkateswaran, S. V. (1979a). Influence of mean zonal motion and meridional temperature gradients on the solar semidiurnal atmospheric tide: A spectral study. Part I: Theory. *Journal of the Atmospheric Sciences*, *36*(9), 1623–1635. https://doi.org/10.1175/1520-0469(1979)036<1623:iomzma>2.0.co;2

Walterscheid, R. L., & Venkateswaran, S. V. (1979b). Influence of mean zonal motion and meridional temperature gradients on the solar semidiurnal atmospheric tide: A spectral study. Part II: Numerical results. *Journal of the Atmospheric Sciences*, *36*(9), 1636–1662. https://doi.org/10.1175/1520-0469(1979)036<1636:iomzma>2.0.co;2

Weimer, D. R. (2005). Improved ionospheric electrodynamic models and application to calculating Joule heating rates. *Journal of Geophysical Research*, *110*(A5), A05306. https://doi.org/10.1029/2004JA010884

Wheeler, M., & Hendon, H. H. (2004). An all-season real-time multivariate MJO index: Development of an index for monitoring and prediction. *Monthly Weather Review*, *132*(8), 1917–1932. https://doi.org/10.1175/1520-0493(2004)132<1917:AARMMI>2.0.CO;2

Wheeler, M., & Kiladis, G. N. (1999). Convectively coupled equatorial waves: Analysis of clouds and temperature in the wavenumber-frequency domain. *Journal of the Atmospheric Sciences*, *56*(3), 374–399. https://doi.org/10.1175/1520-0469(1999)056<0374:CCEWAO>2.0.CO;2

Wu, D. L., Hays, P. B., & Skinner, W. R. (1995). A least squares method for spectral analysis of space-time series. *Journal of the Atmospheric Sciences*, *52*(20), 3501–3511. https://doi.org/10.1175/1520-0469(1995)052<3501:ALSMFS>2.0.CO;2

Yamazaki, Y. (2023). A method to derive Fourier-wavelet spectra for the characterization of global-scale waves in the mesosphere and lower thermosphere and its MATLAB and Python software.

Yang, C., Smith, A. K., Li, T., & Dou, X. (2018). The effect of the Madden-Julian Oscillation on the mesospheric migrating diurnal tide: A study using SD-WACCM. *Geophysical Research Letters*, *45*(10), 5105–5114. https://doi.org/10.1029/2018GL077956

Yiğit, E., & Medvedev, A. S. (2015). Internal wave coupling processes in Earth's atmosphere. *Advances in Space Research*, *55*(4), 983–1003. https://doi.org/10.1016/j.asr.2014.11.020

Zhang, C. (2005). Madden-Julian oscillation. *Reviews of Geophysics*, *43*(2), RG2003. https://doi.org/10.1029/2004RG000158

Zhang, X., Forbes, J. M., & Hagan, M. E. (2012). Seasonal-latitudinal variation of the eastward-propagating diurnal tide with zonal wavenumber 3 in the MLT: Influences of heating and background wind distribution. *Journal of Atmospheric and Solar-Terrestrial Physics*, *78–79*, 37–43. https://doi.org/10.1016/j.jastp.2011.03.005